Unsteady flow mechanisms on airfoils: the extended finite vortex model with applications

R. Liebe
Siemens Power Generation, Mülheim a.d.R., Germany.

Abstract

Fluid dynamics plays a significant role in nature and engineering: locomotion, transportation, power generation, etc. We are familiar with steady flow and the application of classical tools for successful aircraft and turbomachine designs over the last 80 years. Strictly speaking, however, there is hardly any steady flow in real fluids. Friction and inertia—at least locally—cause flow separation, periodic vortex formation and force production. Lift generation remains obscure, if we limit to ideal steady flow. This paper focuses on the mechanisms that govern the unsteady roll-up of vortices along highly curved surfaces. First, flow around fixed bodies is examined, identifying the 'edge flow mechanism' and the secondary role of the 'passive' boundary layer in the formation and shedding of vortices as well as flutter of airfoils (AFs). The trailing edge vortex (TEV) is shown to cause intermittent local suction, which builds up a counterrotating, bound vortex. Next, the arbitrary flow around oscillating AFs is treated for various Reynolds (Re) and Strouhal (Str) numbers. This sheds light on the dynamic stall, the build-up of the leading edge vortex (LEV), the TEV–LEV interaction, and the 'locking in' of frequency/amplitude to the free shedding process. Lift and thrust generation can be maximized by suitable matching. The main body of the paper presents the 'finite vortex model' (FVM): its justification, the dynamic modeling of the fluid–structure interaction, the resulting coupled equations of motion and their solution. The extended FVM concept is successfully validated and applied to both fixed and oscillating AFs over a wide range of scaling parameters Re, Str, f, A_A, covering nature and engineering applications. The finite vortex size $(2a/R)$ is quantified from FVM analyses of pitching/plunging AF experiments; $(2a/R)$ is of paramount importance. Plots of thrust, lift $(C_{\mathrm{T,L}})$ and $(2a/R)$ versus Str results consistently yield hyperbolic type curves, collapsing large test series. The wide FVM potential is evident from simulations of airplane take-offs, drag thrust-regimes from oscillating AFs and from the explanation of high-lift devices: the backflow barrier, Gurney flap, current and newly inspired diverging trailing edge designs. FVM applications to swimming and flying in nature prove the efficient generation and management of large vortices as well as the advantage/limits of approximate thrust equations derived from the conservation of momentum. Analyses quantify the swimming performance of blue whales and the take-off and cruise flight of a large heron.

WIT Transactions on State of the Art in Science and Engineering, Vol 3, © 2006 WIT Press
www.witpress.com, ISSN 1755-8336 (on-line)
doi:10.2495/1-84564-001-2/4b

Final conclusions are derived from all the results, and future experimental and numerical work is proposed.

1 Introduction

Fluid dynamics and the associated physical mechanisms play an important role both in nature and in engineering. High significance can be attributed to the steady and unsteady formation of small and large vortices (see the compilation of van Dyke [1]). Their utilization/control or prevention is often crucial in generating forces/moments in an efficient manner. We can identify a wide range of fluid mechanics applications where lift, thrust and efficiency are to be maximized or overall drag is to be minimized:

Nature

- locomotion in nature, i.e. swimming and flying of animals (fish, insects, bats, mammals and birds);
- distribution of liquids, for instance blood in our body.

Engineering

- transportation in human engineering: ships, airplanes with propellers and jet engines;
- power generation using rotating turbomachinery with vane/blade cascades to convert or transmit and utilize fossil or nuclear energy;
- distribution/pumping of different fluids such as oil, gas, water or slurries, i.e. employing compressors or pumps with rotating vane/blade cascades to generate pressure;
- extraction or transmission of heat: coolers, heat exchangers, boilers/tube banks with vortex shedding.

This paper focuses on the flow physics involved in steady and oscillating motion of airfoils (AFs), fins and wings. Particular emphasis is given to the description of vortex dynamics, vortex interaction with the AF and the generation of lift/thrust forces. The main body of the paper deals with the finite vortex model (FVM) and its further extensions since the first publication by W. Liebe [2].

In spite of several extensions, the FVM still represents a very simple though general tool for approximate analyses. Such analyses may precede and bracket costly Navier–Stokes (NS) investigations, as well as sophisticated experiments. The development of these FVM extensions, their physics with mathematical simulations and their applications were published by R. Liebe since 2002 in [3–7]. All extensions are consequences of earlier findings, continuous discussions with W. Liebe and observations in experiments and nature. Subsequent new FVM analyses agree rather well with published test data on forces and circulation [8]. In addition, the papers [4, 5] cite recent NS results of Gustafson [9, 63], being in accordance with FVM modeling. Last, but not the least, several flow phenomena described in the book by Lugt [11] can be explained with a 2D interaction of vortices. The corresponding FVM predictions are in good agreement with both experimental and numerical findings.

In the first part it is shown that the flow around solid bodies features very different patterns, both in streamlines and vortex formations. The discussion starts with the cross-flow around cylinders. Results of Koopmann [12] and Bublitz [13] on unsteady flow around a fixed cylinder are compared to recent finding. To categorize the different flow patterns and shedding of vortices, it is useful to consider the following physical criteria, which are well described by several authors in [14–17]:

- The domination of inertial forces over viscous forces (Reynolds number).
- The magnitude of centrifugal forces compared to the balancing forces from pressure gradients along curved streamlines (curvature Richardson number or other).
- The steady or periodically unsteady formation of large vortices (size compared to a characteristic length, say the AF chord R).
- The components for propulsion (like an AF) being either solid or elastic; remaining either fixed or executing oscillatory motions relative to the surrounding fluid.
- Possibly random generation of small-scale eddies/turbulence from free shear layers (laminar or turbulent flow).

After briefly describing vortex-based simulation models ranging from early Rayner [18] to Lan [19] (see also [20, 21]), the second part elaborates the FVM itself. The FVM concept has been published by W. Liebe in 1963, [2, 22]. Later on, several joint papers by R. Liebe and W. Liebe [4, 23, 24] followed. Since then, the FVM has been extended for a better modeling of the vortex structure dynamics. This paper, together with [3], describes the current features and extensions of the model. It presents new physical mechanisms with the relevant equations of motion and solution strategies. A wide field of applications is given.

In the third part, general applications of an FVM approximation are presented. Both oscillating as well as a fixed/inclined AF are dealt with. Oscillating AF results include thrust and lift forces. The dynamic interaction of the trailing edge vortex (TEV), the bound vortex BV [including the leading edge vortex (LEV)] and the AF itself is illustrated with experiments and discussed in detail. Recent results (see [3]) are concerning the fixed AF with the vortex size and the detachment frequency of near-field finite vortices [6].

The fourth part presents typical applications of both the TEV/BV, LEV interaction and the use of the FVM in engineering as well as in the biology of swimming and flying. Several ideas proposed by W. Liebe in [22] were also investigated by Bechert [25, 26] and by Meyer [27] and Rechenberg [28] later on. Practical applications range from micro air vehicles [29] to modern fighter jets [30]. Qualitative explanations are given for the computational fluid dynamic (CFD) findings of Mehta [31] and the tests of Vermeulen [32] as well as McAlister [33] and Carr [34]. FVM applications with prescribed AF kinematics typically result in time-dependent forces, AF circulation and power requirements. Engineering FVM simulations are performed to predict the pitching experiments [2] and the plunging behaviur from AF oscillation tests by Lai *et al.* [8, 35]. Also, a fixed aircraft and turbomachine AF is simulated with an FVM representation [3, 6]. Then alternative AF designs are proposed for high lift and/or delayed stall [36]; they are compared with conventional concepts. In this context, it is interesting to take a look at several unusual wing profiles suggested by Kasper [37] in 1978.

Finally, applications in nature address swimming—especially the common caudal fin propulsion in fish—as well as flying in birds.

Last but not least, up-to-date experience with the FVM, findings from applications and open points are summarized. The conclusions include both the Limits and the potential of the FVM. Furthermore, future experimental and numerical work is proposed.

2 Operating regimes in fluid dynamics

To separate and analyze the dominating physical flow mechanisms in fluid dynamics, it is useful to distinguish the following operating regimes indicated in Figs 1 and 2. See the work of Freymuth [9, 38], Durst [39], Dickinson [40, 41], Kawachi [42] and Hedenström [10].

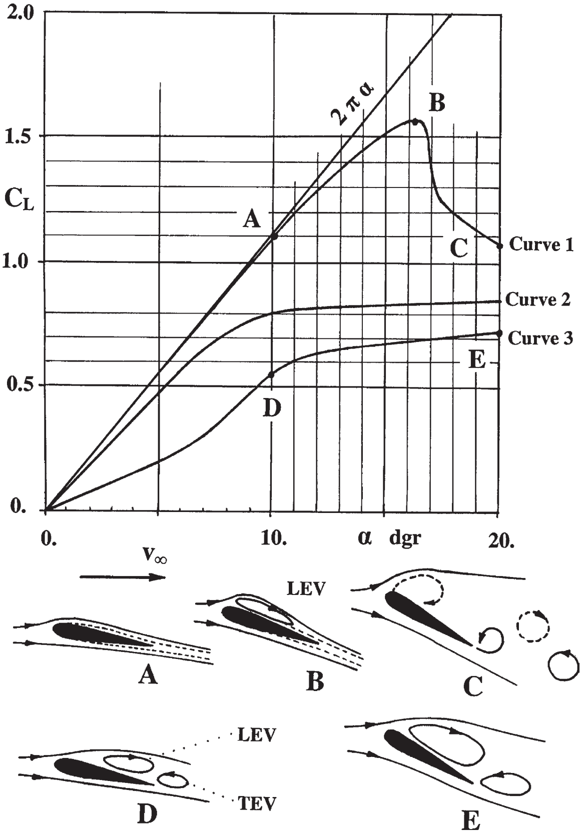

Figure 1: Flow around a fixed, inclined AF: the effects of viscosity (Re number) and of global flow separation (angle of attack α, 'curvature' of AF). (A–E) Curve 1: NACA 0012, with high Re $= 10^6$. The theoretical curve for a flat plate is $2\pi\alpha$. Curve 2: Flat plate, 5% thickness, with low Re $= 4.0 \times 10^3$. Curve 3: NACA 0012, with low Re $= 4.0 \times 10^3$. Test results redrawn from [14, 15].

A. *Flow around fixed bodies*
  A1. High Re numbers
    - Flow without separation
    - Flow with separations
      — Globally steady flow pattern
      — Globally unsteady flow pattern
  A2. Low Re numbers
B. *Flow around oscillating bodies*
  B1. High Re numbers
  B2. Low Re numbers

Figure 1 depicts different operational flow regimes around fixed AFs, such as an airplane wing, in a constant, free-stream velocity v_∞; it shows the effect of fluid viscosity and global separation on the C_L performance and the associated flow structure. Separation may finally lead to periodically unsteady or fully irregular vortex patterns. The test data given are redrawn from [14, 15].

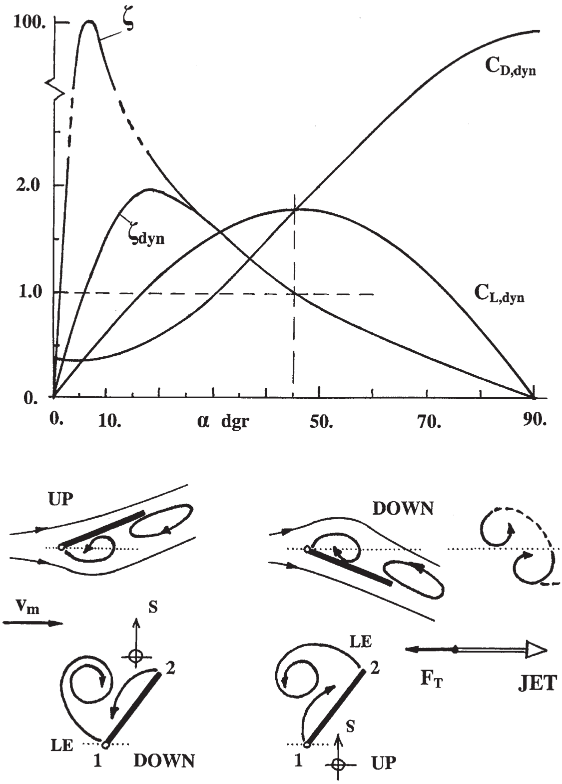

Figure 2: Flow around an oscillating AF with medium Reynolds numbers (typical: $\mathrm{Re}_{\mathrm{vmax}}$ ca. 10^4). Top: Measured dynamic lift and drag—$C_{\mathrm{L,dyn}}$, $C_{\mathrm{D,dyn}}$—as well as corresponding dynamic 'profile quality' $\zeta_{\mathrm{dyn}}(t) = (C_{\mathrm{L,dyn}}/C_{\mathrm{D,dyn}})$ for a flat plate as a function of the instantaneous angle of attack $\alpha(t)$. Data for pure pitching redrawn from [40]. Static curve: $\zeta(\alpha_{\mathrm{static}})$. Middle: Pure pitching $\varphi(t)$ around the leading edge with vortex and wake patterns as well as a resulting thrust force $F_{\mathrm{T}} > 0$ with $v_\infty = 0$; $v_{\mathrm{m}} \neq 0$. Bottom: Flat, symmetric AF in hovering 'model one' oscillating with a combined 2D motion $s(t)$ and an advancing φ $(t + \pi/2\omega)$. Typical vortices redrawn from NS data [9].

Figure 2 shows the dynamic profile quality ζ_{dyn} (α_{dyn}) of a simple flat plate, redrawn from the tests of Dickinson [40]. The maximum ζ_{dyn} is ≈ 1.9, compared to the static $\zeta(\alpha_{\mathrm{stat}})$ of a good airplane profile with maximum ζ up to ≈ 100, due to its much lower drag. In addition, Fig. 2 shows entirely different flow patterns, developing around an oscillating AF (see [16, 17]). A much higher C_{L} level ($C_{\mathrm{L,dyn}} \approx 1$–$5$) and also a higher C_{D} level ($C_{\mathrm{D,dyn}} \approx 1$–$2$) results from the unsteadiness.

Typical for all these cases is the formation of two lagging, counterrotating vortices, which—after a 'forced detachment'—generate characteristic wakes. Corresponding studies are reported from Panda *et al.* (see also [8, 10, 38, 43, 44]). Wakes can be visualized as 'footprints' of prior events, i.e. the active vortex attachment phase, where the forces were generated. The wakes may be either of the classical (drag) or of the 'reverse' (thrust) von Karman type. Their pattern depends on details of the vortex formation and interaction within the TEV/BV, LEV system.

For the characterization and analysis of the time-dependent vortices we have to distinguish the different oscillation kinematics, as well as two generally different levels of Re numbers: The mean flow-through velocity v_m (first approximation: v_m = free stream + 1/2 mean jet velocity) with the corresponding $\mathrm{Re} = \mathrm{Re}_\mathrm{vm} = (v_\mathrm{m} R/\nu)$ and the maximum oscillating velocity of the trailing edge v_max [for pure pitching around the leading edge: $v_\mathrm{max} = (\varphi_0\, \omega\, R)$] with the corresponding $\mathrm{Re}_\mathrm{vmax} = (v_\mathrm{max} R/\nu)$ (see also [7, 45]).

3 Flow around fixed bodies

Flow around a fixed AF is considered first. Figure 1 shows a subsonic, incompressible flow with $\mathrm{Ma} \leq 0.7$ around an inclined AF. This AF with a chord R is held fixed relative to the surrounding constant free-stream velocity v_∞. As an example, the lift coefficient C_L is shown—$C_\mathrm{L} = F_\mathrm{L}/(\rho/2\, v_\infty^2 RB)$—as a function of the angle of attack α ($\alpha \approx 0$–$20°$) and the Re number, $\mathrm{Re} = (v_\infty R/\nu) = \mathrm{Re}_\mathrm{R}$ with $\mathrm{Re} \approx 10^3$–10^6. Experimental data is given for a symmetric NACA 0012 AF (12% thickness), [14, 15]. This example is chosen to demonstrate the effects of fluid viscosity and global flow separation. Also given are schematic sketches of the characteristic flow patterns from experiments.

The curve 1 with the point A is typical for the operation of an aircraft wing or a turbomachine profile with a high Re number ($\mathrm{Re} \approx 10^6$), a small angle of attack ($\alpha \approx 10°$–$15°$), high lift ($C_\mathrm{L} \approx 0.6$–1.4) and a very low drag C_D. It is also characterized by dominating inertial forces, thin boundary layers δ and attached flow conditions. Therefore, this regime can be well described by steady, inviscid potential or panel methods, in combination with boundary layer analyses. Besides that, recent NS analyses—for instance by Denos, [46]—show a high frequency vortex shedding from the trailing edge. This local, periodically unsteady flow is also found in recent experiments of Zheng [47]. In spite of those findings for the AF performance around point A, the flow regime can be treated as 'globally' steady.

Next, curve 1 with point B (Fig. 1) represents a very high C_L from enhanced vortex lift due to the formation of a large, stable, well-trapped LEV, which acts as an enhanced, BV around the AF [15, 37]. For safety, this narrow regime is usually avoided in commercial aviation, to protect against sudden stall, i.e. flow separation with a catastrophic drop of lift (see [33, 48] and Fig. 7A and B). The resulting vortex patterns are mostly globally steady.

Finally, curve 1 with the point C involves highly unsteady flow conditions due to massive, time-dependent flow separation, periodic formation of large dynamic stall vortices (LEV), noise as well as LEV–TEV–blade interaction (see [48] and Fig. 7A and B). This regime is characterized by 'flutter' with a sudden, subsequent drop and time variation of C_L, plus a steep rise of C_D. Flutter may occur on helicopter blades; it is strictly avoided in commercial aircraft and turbomachine design [15, 49]. However, highly maneuverable aircraft or fighter aircraft, may temporarily enter the regime around the points B to C. (See also the publications of Kawachi [42] and Platzer [16].)

The curves 2 and 3 with the points D and E in Fig. 1 are for very low Re numbers ($\mathrm{Re} = 4.0 \times 10^3$) with dominating viscous forces, the formation of large, mostly steady LEV and TEV (see the numerical CFD results of Durst in Fig. 7C from [39]). The low C_L, high C_D values are usually constant.

Such vortices are utilized for mixing and in process engineering. They are found around slowly oscillating fins or wings in nature as well. Typical vortex structures can be seen from the NS results of Wu [50]. In this regime it is difficult to define a 'boundary layer' because we are faced with large viscous zones. Very interesting in this context are the experimental findings on the dynamic LEV formation in hovering dragonflies. Currently there are controversial discussions on the stabilization of this LEV, and whether spanwise flows enhance it or not (see [44, 51, 52]). With the extended

FVM concept it is possible to explain this LEV stabilization. Explanations can also be given for a number of experimental findings reported in [41, 51–53]. More details are given in Section 5.

3.1 The edge flow mechanism

Figure 3 shows the so-called ‘edge flow mechanism’, taken from the visualizations of Eck [49] (see also [3]). This is a very common phenomenon when a fluid with a normal flow velocity

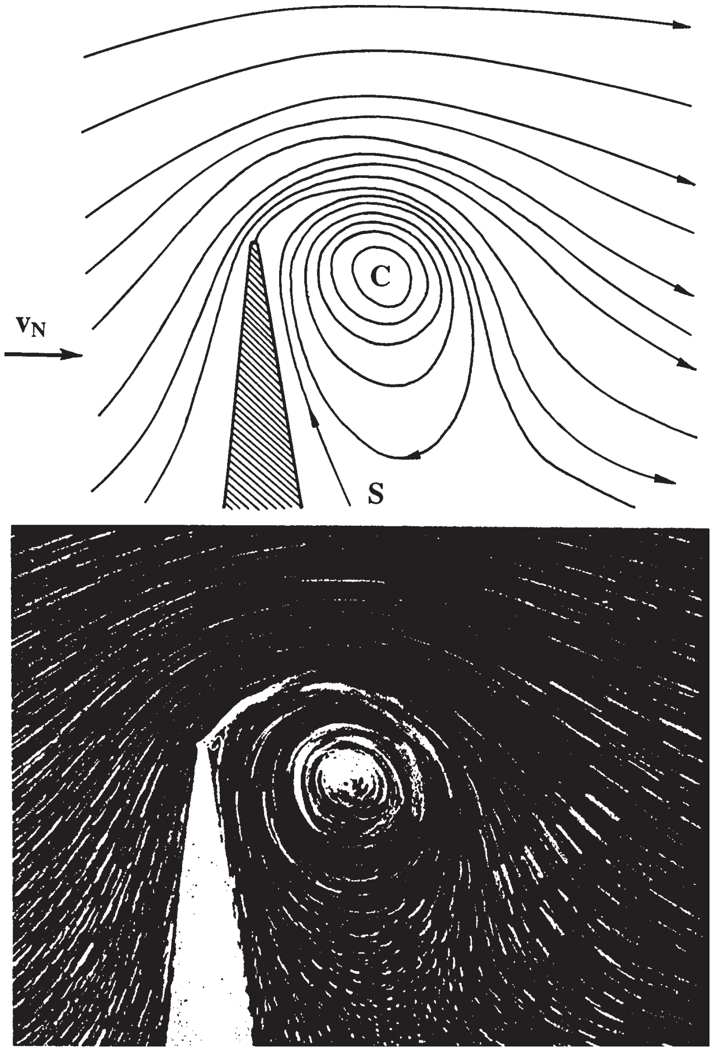

Figure 3: The ‘edge flow mechanism’ [2]. The bottom part shows flow visualization experiments taken from [49], depicting the 2D roll-up of a large vortex (may become steady, or periodically unsteady). It is formed behind a sharp-edged wedge after a sudden flow separation. In the top part, streamlines from below are redrawn, showing the normal velocity v_N, the low pressure ‘solid core’ C (sink) and the one-sided suction zone S.

v_N hits a sharp edge or a strongly curved surface (curvature $1/R_c$), so that the centrifugal forces would dominate over the pressure forces. Due to its inertia, the fluid cannot follow the local curvature $1/R_c$. It separates from the surface, and the one-sided suction S bends the streamlines into a large vortex. The corresponding limit may be characterized by a curvature Richardson number $\mathrm{Ri} = (v/R_c)/(\mathrm{d}v/\mathrm{d}y)$ for curved streamlines [54]. Possibly, also a suitable parameter for the gradient $(\mathrm{d}v/\mathrm{d}y)$ across the thickness of the boundary layer (BL) determines this limit. Downstream, the separation zone the BL becomes 'free' and forms an unstable shear layer. (See the test results of Pierce [55], given in Fig. 6A).

For a while, the vortex in Fig. 3 remains attached to the edge, being fed with fluid as long as the suction S is maintained. This is a self-limiting process that controls the vortex roll-up, until it reaches a stable 'size' with a finite net flow-through m_{in}. For continuity, this m_{in} then has to equal an m_{out} (likely around the vortex periphery). The associated TEV mechanism has been postulated by W. Liebe, as a result of his early in-flight flow studies on stalling fighter planes back in 1938 (see also [25]). The description is given in his much later publication [22] on the generation and breakdown of lift.

Figure 3 does not show any stagnation point on the lee side of the edge, and there is no flow division with a dividing shear layer or discontinuity surface, as currently thought (see sketches of Prandtl in [56]).

3.2 Vortex formation

The very fruitful and eye-opening controversy between Ahlborn [57] and Prandtl [56] back in 1927 is little known today. This historical discussion centered around the root causes of vortex formation in fluids and the role of the BL in that context. On visualizing and analyzing flow experiments around still and rotating cylinders (Magnus effect), Ahlborn could not agree with Prandtl's separation theory. Prandtl based his separation and vortex formation theories primarily on an 'active BL'. He postulated that the BL is able to flow back due to a global, reverse pressure gradient. Ahlborn, however, could not imagine an active BL since, by definition, it has a low velocity level. Because it is very thin and 'passive', it is driven by the higher-velocity external flow. So he argued that flow separation is initiated by the 'active' external, inertia-based high-velocity field. The author follows Ahlborn here in saying that this high-energy flow cannot follow an edge or a highly curved flow path. Then spiraling streamlines form a vortex, with centrifugal forces and pressure forces balancing each other. Due to this balancing, a potential-type vortex with $(v_\varphi r) =$ constant and a 'solid core' are formed [3].

Even after about 80 years, this controversy does not seem to be fully resolved. In addition, there is the old paradox: How can vorticity originate in an inviscid fluid, despite the classic theorems of Helmholtz and Thomson (according to these theorems this is impossible)? To overcome, this paradox, Prandtl introduced the 'vortex-sheet' or the 'discontinuity (shear) layer'. The common understanding today still follows the Prandtl school, according to which vortex formation is primarily controlled by an unstable, 'wavy' discontinuity or shear layer, emanating from the BL at the separation point on the body surface [56]. The majority of today's views also follow Prandtl in saying that reverse pressure gradients can force the BL to flow back and upstream along the wall.

The author believes that both theories—Ahlborn and Prandtl—do not exclude each other: in general the primarily 'active part' in the formation of large vortices is the inertia-dominated external domain of the flow field. Nevertheless, viscosity-dominated flows may develop in a rather complex manner as shown by the NS results of Jian *et al.* [58]. Most cases, however, are of the type depicted in the visualization of Fig. 3, which clearly indicates a nearly tangential or spiral in-flow velocity into the primary vortex. In other types of flow, frequently, reverse pressure gradients do cause a backflow of fluid close to the curved walls. The BL underneath, however, is just 'dragged along' by the neighbouring flow (see Fig. 20). On the other hand, there are cases where the passive BL produces small, local vortices, emanating from the unstable free BL. This can be seen from the experiments [55], cited in Fig. 6. Once the BL is free, it forms an unstable shear layer, which may break up into smaller spiral vortices, as confirmed by the NS results of Wang *et al.* [59]; these are also shown in Fig. 6B. The small spiral vortices are controlled by, and thus arranged along, the stronger spiral in-flow stream lines. The streamlines form the large primary vortex attached to the trailing edge of the moving AF.

3.3 Flow around fixed cylinders and AFs

The edge flow shown in Fig. 3 can be visualized as a 'degenerated' form of a general, 'symmetric' cross-flow around a fixed body. These general fixed body flows can be characterized by the

- formation of two counterrotating vortices (of equal/opposite strength of circulation), and
- existence of two stagnation points on the luff and lee side.

Similar to one half of a fixed, rectangular plate oriented 90° to a free stream, the above 'degeneration' of the simple edge flow is due to a nonsymmetric flow field.

Now the 'complete or symmetric', general flow around fixed (oscillating) bodies is considered. The developing flow patterns highly depend on the involved Reynolds (and Strouhal) numbers. The resulting near-field flows and wakes are made up from stationary, periodically unsteady or fully turbulent vortex structures. As an example, Figs 4 and 5 indicate cross-flow visualizations around fixed circular cylinders (diameter D, free-stream cross-flow v_∞) for different $\mathrm{Re_D} = (v_\infty D/\nu)$, leading to either a laminar, drag-type von Karman vortex street or fully turbulent conditions. The flow phenomena addressed give insight into the

- types of steady/unsteady streamlines or streaklines that form around the cylinder;
- roll-up of steady or periodically shedding vortices behind the cylinder;
- resulting time-dependent static pressure distribution and positions of stagnation points;
- generation of constant or time-dependent forces (magnitude, orientation) acting on the cylinder.

3.4 Vortex shedding from fixed cylinders

Figure 4 depicts three selected photographs of characteristic vortex wakes from van Dyke [1] and Koopmann [12], demonstrating low Re number flows ($\mathrm{Re_D} \leq 200$). The light-sheet technique is used in conjunction with smoke or particle seeding to visualize the streamlines or streaklines. Figure 4A indicates an upper limit, being around $\mathrm{Re_D} = 41.0$: the range $\mathrm{Re_D} \approx 40$–150 ($\mathrm{Str_D} \approx 0.12$–0.17) can be considered as 'stable'; it marks the transition from steady/stationary 'standing' vortices to periodically unsteady vortex formation. Shedding occurs from $\mathrm{Re_D} \approx$ 150–300. The resulting laminar von Karman vortex streets are depicted in Fig. 4B and C.

The dimensionless vortex shedding frequency f_{VS} is expressed by the Strouhal number $\mathrm{Str_D} = (f_{\mathrm{VS}} D/v_\infty)$, denoting the natural, 'free' shedding time scale. $\mathrm{Str_D}$ is not independent, and the characteristic function $\mathrm{Str_D}$ ($\mathrm{Re_D}$) is of great importance in engineering. Experiments indicate that a practically constant shelf-value of $\mathrm{Str_D} = 0.21$ is attained, approaching $\mathrm{Re_D} \approx$ 1000–5000. (Details are found in Schlichting [60].) A completely irregular, fully turbulent condition is reached above $\mathrm{Re_D} \geq 5000$; there is no shedding anymore.

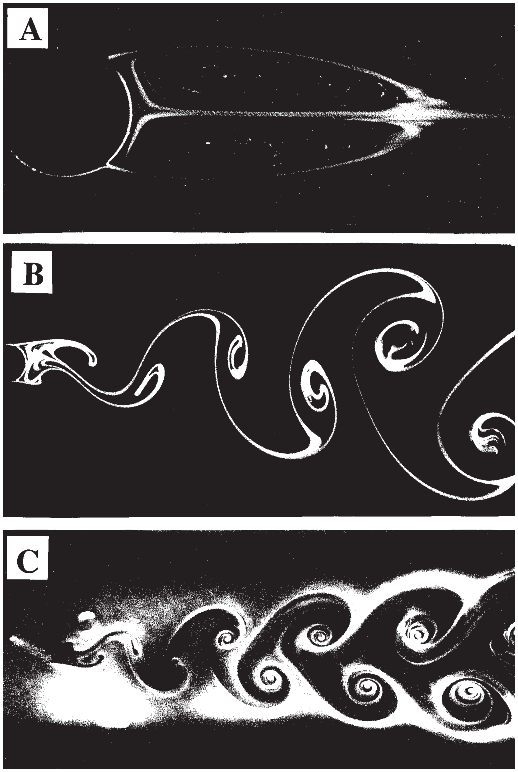

Figure 4: Vortices behind a fixed circular cylinder (1)—flow from left to right—$\mathrm{Re_D} \leq 200$, with laminar wakes. (A) Steady, 'standing' vortex pair at the limiting $\mathrm{Re_D} = 41.0$ (no shedding, $f_{\mathrm{VS}} = 0$) [1]. (B) Periodically unsteady flow at $\mathrm{Re_D} = 140$, with $\mathrm{Str_D} = 0.210$ and a shedding frequency $f_{\mathrm{VS}} = 1.4\,\mathrm{Hz}$ ($D = 0.010\,\mathrm{m}$), photo from [1]. (C) Periodically unsteady flow at $\mathrm{Re_D} = 200$, $\mathrm{Str_D} = 0.192$ and $f_{\mathrm{VS}} = 28.0\,\mathrm{Hz}$ ($D = 0.0047\,\mathrm{m}$), photo from [12].

Figure 5 indicates typical examples of vortex structures for nearly and fully turbulent wakes with $\mathrm{Re_D} > 3000$. The laminar character of the wake flow progressively deteriorates upstream until it reaches a completely irregular pattern. It can be seen, however, that the turbulent wake still swings from side to side, with the rear stagnation point (RSP) switching around the symmetry line.

In general the RSP may move away from the lee surface of the cylinder into the near-wake fluid. The 'free RSP' (saddle point) also performs transverse jumps across the symmetry line. The jumps are synchronous with the oscillations of both the separation points and even the front stagnation point (FSP). These unsteady motions are due to the interaction of the one-sided attached vortex with the oncoming cross-flow. The involved instability is likely to be controlled by the force imbalance and phase delays between centrifugal forces and those from pressure gradients. As a consequence, the entire flow field oscillates around the cylinder, and so do the resulting fluid forces F_2 (normal) and F_1 (in-line). The direction of the force vector $F = (F_1; F_2)$ always points to the growing vortex, occurring last. Following Bublitz [13], this can be considered as an 'unsteady Magnus effect'. Such unsteady forces have an important significance in engineering, and there are means to influence or interrupt the vortex formation, for instance, by splitter plates and/or fences.

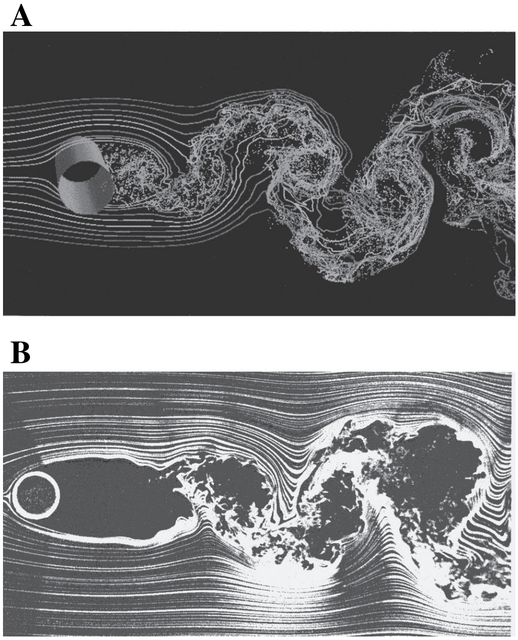

Figure 5: Vortices behind a fixed circular cylinder (2)—flow from left to right—$\mathrm{Re_D} > 3000$, with nearly or fully turbulent wakes. (A) Nearly turbulent wake, streaklines at $\mathrm{Re_D} = 3900$ with $\mathrm{Str_D} = 0.210$, i.e. still vortex shedding with a frequency of $f_{\mathrm{VS}} = 129.4\,\mathrm{Hz}$ ($D = 0.010\,\mathrm{m}$) [39]. (B) Fully turbulent wake at $\mathrm{Re_D} = 10\,\mathrm{K}$ [1].

3.5 Accelerated edges

Flows around moving bodies add more complexity to the resulting unsteady velocity field. The fluid–structure interaction and force generation depends on additional factors, such as:

A. kinematics of structural motion: level of acceleration, oscillation frequency/amplitude;
B. the moving structure may be a rigid or an elastic body;
C. the degree of physical coupling between motions of the structure and of the fluid: either purely prescribed structural motion (not depending on fluid forces), or structural motion being affected by the flow-induced forces (and vice versa).

Propulsion elements in nature (flapping wings of birds, oscillating fins of fish) very often change their mode of force generation, according to the instantaneous needs. In addition, nature never operates fins or wings completely rigidly; two mechanisms are efficiently combined: the primary active kinematics and the hydro- and aeroelastic feedback.

Figure 6 shows a clear example of fully prescribed kinematics: a plate with unsteady flow developing around accelerated, differently shaped edges in still air. Flow phenomena are controlled by a 'dynamic edge flow mechanism' (compare Fig. 3). Typical effects are observed: a primary and a secondary vortex formation, again with a tangential in-flow towards the primary vortex. The overall pattern and even detailed flow structures from these experiments [55] are confirmed numerically by the NS simulations [59].

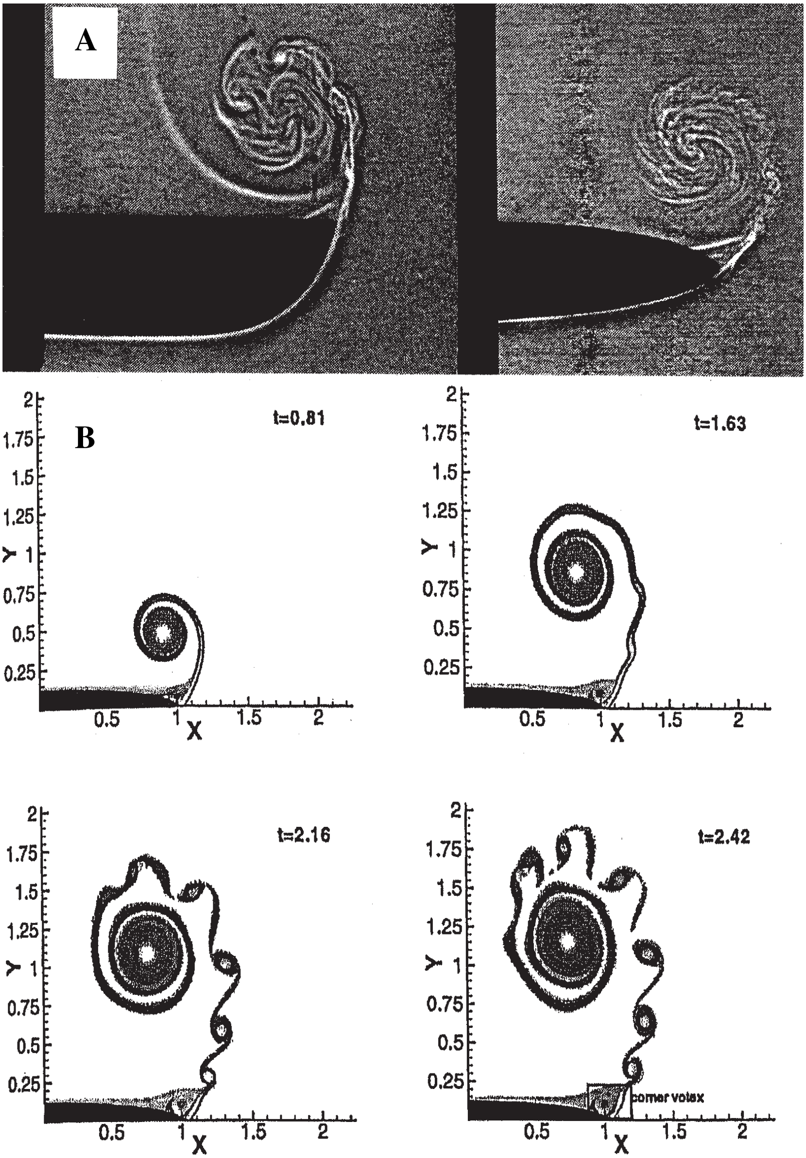

Figure 6: Vortex systems from accelerated ‘shaped’ edges of airfoils, unsteady flow from bottom to top. (A) Experiments behind accelerated circular plates with ‘shaped’ edges. Maximum air flow with $v_{\max} = 7.0\,\mathrm{m/s}$ ($\mathrm{Re}_{v\max} = 11.2\,\mathrm{K}$). Tangential in-flow from the lee side towards the vortex core as well as vortex substructures along the spiral streamlines of the primary vortex are visible [55]. (B) NS simulation of the unsteady flow around the transversely accelerated edges of an elliptic AF; small spiral vortices are formed around the primary vortex [59].

Contrary to Fig. 6, a large group of problems involves aeroelastic coupling and 'flutter' phenomena: structural displacements cause spring-, damping- and inertial-type fluid forces as a 'feedback' from the fluid. Flutter problems—arising from so-called 'dynamic stall' (see Section 4.1 and Fig. 7)—have a very high significance in engineering [61]:

- Self-excited wing vibrations with catastrophic failures in aircraft engineering.
- Helicopter rotor blade/wake interaction with noise and dynamic stall loading. The slender elastic rotor blades require a 'flutter-resistant' design.
- Flutter excitation of slender blades/vanes in steam and gas turbines [17].
- Unstable fluid–structure interaction in turbomachines: rotating impeller blades/vanes or propellers with the surrounding fluid flow. High forces and low damping often cause failures.

In these cases, significant fluid energy is transmitted to the structure, which often has limited structural damping. The resulting self-excited vibrations frequently lead to 'explosive' structural failures.

3.6 The trailing edge vortex and the bound vortex

The key mechanism in flows around moving or oscillating AFs is the unsteady roll-up of large vortices, which are able to generate significant forces [6]. This holds for both classes of problems: the 'passive' aeroelastic case with energy transmitted from the fluid to the structure as well as the 'active' propulsion case with an energy transmission from the structure to the fluid.

Fixed as well as oscillating AFs generally involve the formation of two time-dependent vortices: The primary trailing edge vortex (TEV) and the counterrotating bound vortex (BV), which sometimes manifests as a leading edge vortex (LEV). Propulsion in nature is achieved by an 'adapted' strong AF motion with a delicate management of high circulation vortices [41]: net positive thrust forces > drag. Lift forces > animal weight.

The forces remain high, as long as the generated vortices are strong and closely attached to the AF for a long period of time. The author believes that the bulk part of force production is achieved from the near-field interaction between the attached TEV, and a driven counterrotating BV around the AF (see Section 5). Far-field effects from distant, detached vortices in the wake are believed to be secondary. Typically the TEV stays attached to the trailing edge. The BV—and as part of it—the LEV are positioned between the two stagnation points: the FSP and the RSP. Thus the BV system is bound to the AF; it can produce a transverse force during the 'active' residence time, before it detaches. The primary TEV apparently drives the other ones across the rear stagnation line; they interact though their timescales of roll-up and the time for picking up strength differ. A similar interaction takes place in flows around cylinders (Figs 4, 5), but vortex formation and interaction around AFs are stronger due to significant differences:

- a rounded (blunt) leading edge, combined with a sharp trailing edge of the AF profile [23];
- often the nonsymmetric AF geometry: profile camber, thickness, etc. [14];
- 'skewed' kinematics with a phase delay between rotation and translation of the AF [40].

In the following (Sections 4 and 5) we focus on oscillating AFs, which are most important in engineering as well as in nature. In this paper we restrict to the general case, characterized by

- arbitrary, fully prescribed AF kinematics, mostly 2D harmonic motion;
- oscillations with arbitrary frequencies and amplitudes;
- superimposed arbitrary free-stream velocities (zero or nonzero);
- rigid AFs.

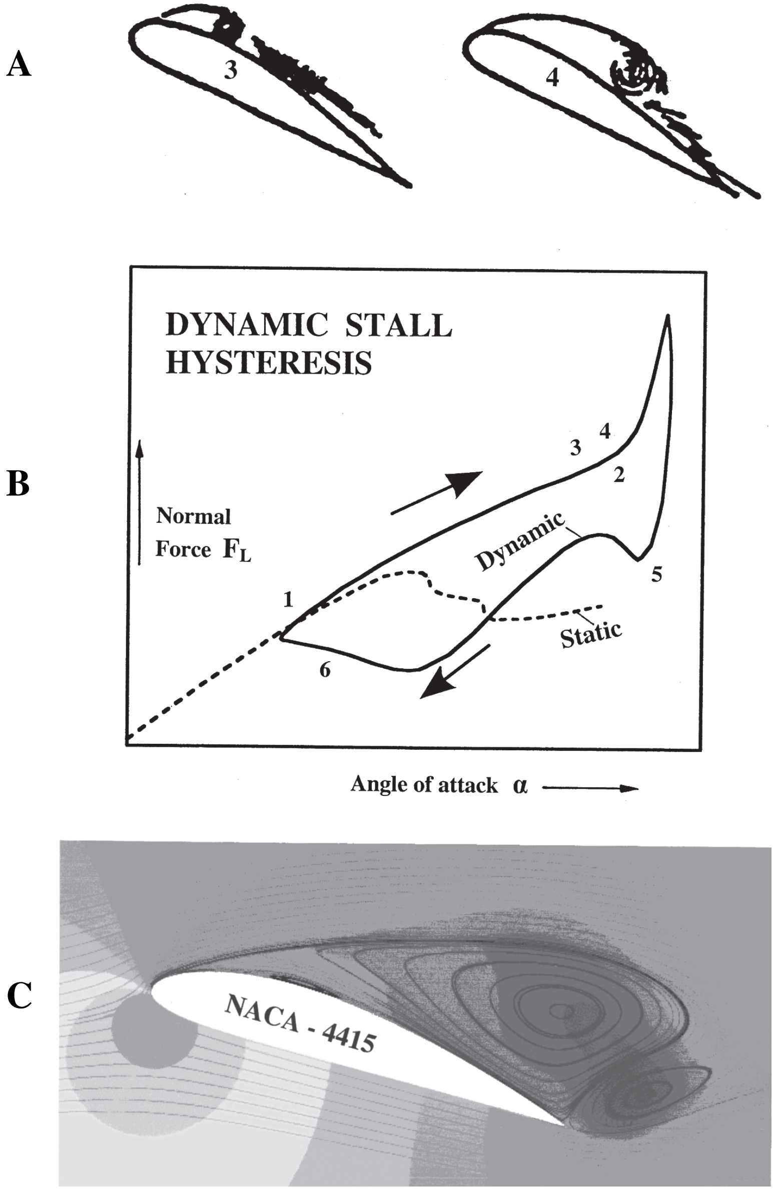

Figure 7: Dynamic stall from an NACA 0012 test is contrasted to a large eddy simulation (LES) of a highly viscous flow around a fixed, inclined NACA 4415. (A) High $\mathrm{Re_R} = 2.5 \times 10^6$ in air, $R = 1.22\,\mathrm{m}$, dynamic $\alpha_{\mathrm{DS}} = 25°$. Deep dynamic stall with 'forced' BV, LEV formation/detachment and flat, strong TEVs at a $\mathrm{Str}_\infty = 0.15$ ($f_{\mathrm{OS}} = 3.98\,\mathrm{Hz}$). (B) Resulting measured transverse force ('lift') $F_\mathrm{L}(\alpha)$ with stall hysteresis and dynamic overshoot. Phases: 1, static $\alpha_{\mathrm{SS}} \approx 15°$ exceeded; 2, flow reversal on the SS; 3, formation of BV, LEV/stabilization by TEV; 4, moment stall; 5, full stall and 6, Reattachment of BL. All redrawn from [48]. (C) Low $\mathrm{Re_R} = 20 \times 10^3$, fixed AF, $\alpha = 18°$. Viscous flow regimes with steady, separate vortices TEV/BV, LEV. Steady static pressure lines, no shedding. LES results from [39].

4 Flow around oscillating bodies

The superposition of external and near-body flow introduces strong nonlinear effects, as long as both independent velocity levels (v_m and v_max of the oscillating AF) are not too far off ($\mathrm{Re}_\mathrm{vm} \approx \mathrm{Re}_\mathrm{vmax}$). Generally, this is the case for large frequencies f_OS and amplitudes φ_o, s_o; then the velocity ratio is around $f = (v_\mathrm{m}/v_\mathrm{max}) \leq 5$. Similarly, the fixed AF develops nonlinearities for larger $\alpha \geq 20°$. In both cases, we expect larger, normal velocity components v_N with subsequent vortex generation.

Additionally, if sufficient time is available for larger vortices to roll-up, then the primary pair of strong TEV/BV, LEV can form and generate forces during their residence time Δt_a. To meet the natural timescale, the oscillation frequency f_OS should not be too far off the free shedding f_VS, (see the vortex visualizations in [9, 38]). In this context it is interesting to note that nature operates fins and wings mainly in this 'matched resonance' range with $f_\mathrm{OS} \approx f_\mathrm{VS}$, preferring $\mathrm{Str}_\mathrm{A} \approx 0.1$–$0.2$ (see Section 8 and also [86]). This range is typical for the efficient generation of large, beneficial forces. If, on the other hand, the forced f_OS works 'against' the natural f_VS, say $f_\mathrm{OS} \approx 2f_\mathrm{VS}$, then parasitic, high drag forces prevail (they roughly double), and the wake pattern changes to a symmetric one [11].

4.1 Dynamic stall

Stall (static stall) refers to the onset of periodically unsteady flow around a fixed, inclined AF. It is initiated by a sudden flow separation from a critical, large $\alpha = \alpha_\mathrm{SS}$ on (Fig. 1, curve 1, point C with $\alpha_\mathrm{SS} = 20°$). The AF is held stationary. Subsequent natural vortex shedding (f_VS) generates the typical drag-type wake, the regular von Karman street (Section 3.4, Fig. 4).

Superimposing AF oscillations, say $\varphi(t) = \varphi_\mathrm{m} + \varphi_0 \sin \omega t$ delays the flow separation, and the vortex detachment is forced to follow $f_\mathrm{OS} = \omega/2\pi$. Figure 7A and B indicate this 'dynamic stall' situation with $\mathrm{Str}_\infty = 0.15$ (or $f_\mathrm{OS} = 3.98\,\mathrm{Hz}$). The experimental finding with alternating TEV/BV generation is taken from [48]. The dynamic stall hysteresis $F_\mathrm{L}(\alpha)$ corresponds to $\mathrm{Re}_\mathrm{R} = 2.5 \times 10^6$ in air, and the beneficial delayed stall shifts the critical angle α from the static $\alpha_\mathrm{SS} = 15°$ to the dynamic level $\alpha_\mathrm{DS} = 25°$. The large LEV bubble in Fig. 7A is believed to be stabilized by the counterclockwise, small but strong TEV (Figs 3, 8 and 9). This enhances the suction and the mean F_L over an extended Δt_a from the delayed separation. 'Stabilization' here means strengthening of the peripheral (BV, LEV) velocity and protecting the low-pressure LEV core from fluid in-rush and force breakdown, respectively. The phases 1–6 in Fig. 7B [48] are typical for this phenomenon, which often leads to destructive flutter.

In contrast to the dynamic stall, now Fig. 7C depicts the steady viscous flow regime with a stationary pair TEV/BV, LEV around the NACA 44015 profile. This LES result is taken from [39]; it represents the typical flow at $\alpha = 18°$ and a low $\mathrm{Re}_\mathrm{R} = 20 \times 10^3$.

4.2 Oscillating AFs

Dynamic stall and periodic TEV/BV, LEV interaction effects get more pronounced with higher frequencies ($\mathrm{Str}_\infty = f_\mathrm{OS}\, R/v_\infty$) and amplitudes [$A_A = (s_\mathrm{o}/R)$ or φ_o)]. Corresponding NS results from Mehta [31] are shown in Fig. 8: a purely pitching (quarter chord), modified NACA 0012 AF with $\mathrm{Re}_\mathrm{vmax} = 4115$, $\mathrm{Str}_\infty = 1.0$ ($R = 0.092\,\mathrm{m}$, $f_\mathrm{OS} = 9.34\,\mathrm{Hz}$, $v_\infty = 0.859\,\mathrm{m/s}$, $\varphi_\mathrm{o} = \varphi_\mathrm{m} = 10°$) superimposed by laminar free-stream conditions with $\mathrm{Re}_\mathrm{R} = 5000$. Figure 8 clearly depicts

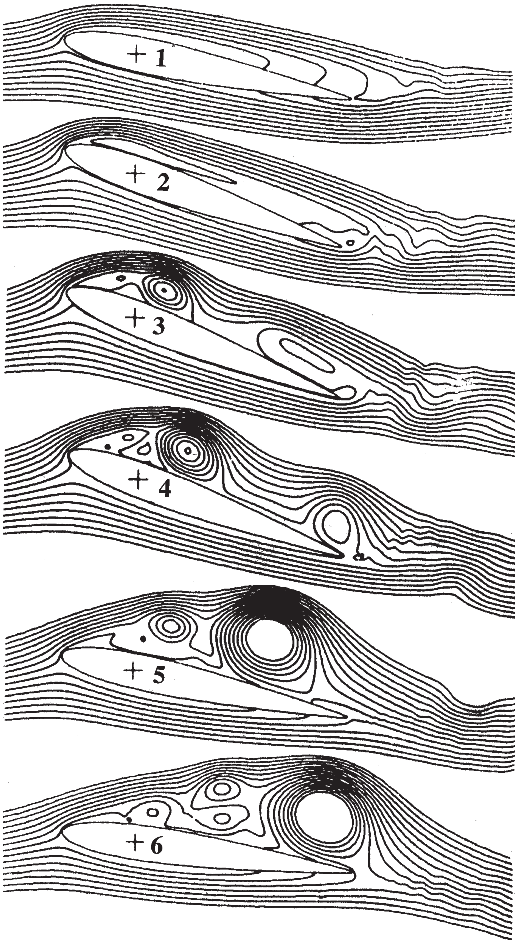

Figure 8: Pitching AF at $\mathrm{Re_R} = 5000$, $\mathrm{Re_{vmax}} = 4115$, $\mathrm{Str}_\infty = 1.0$ and $\varphi_\mathrm{m} = 10°$, $\varphi_0 = 10°$, laminar NS analyses from [31] with streamlines, showing growth and 'forced' detachment of TEV/BV, LEV systems (pure pitching around ¼ chord point, detachment of two vortices (LEV, TEV) per half cycle $T/2 = 1/2f_\mathrm{OS}$). The oscillation frequency is $f_\mathrm{OS} = 9.34$ Hz, 'locked-in' to the natural shedding frequency f_VS; $R = 0.092$ m ($\varphi = \varphi_\mathrm{m} + \varphi_0 \sin \omega t$, instant positions 1, $\varphi = 11.04°$; 3, $\phi = \varphi_\mathrm{max} = 20°$; 6, $\varphi = 7.68°$).

the pronounced formation and detachment of a smaller, strong TEV and a large, clockwise LEV. Six instant AF positions φ_1–φ_6 are shown with streamlines, covering $T/2 = 53$ ms.

According to the author's opinion there are three main effects contributing to a strong TEV/BV, LEV system:

- Matching the AF dynamics with the fluid motion.
- Suitable choice of Str_∞ and A_A for a strong, TEV-driven suction S, which is equivalent to a bound vortex BV around the AF (Figs 3 and 10). As part of the BV, an LEV may develop at larger α. The BV, LEV system generates the F_L.
- Extension of the BV residence time Δt_a enhances the mean F_L level.

The findings in Fig. 8 are in close agreement with other CFD results such as in [9, 17, 39, 50, 58, 61–63]. Also, most of these NS computations are confirmed by experimental findings such as in [8, 29, 33, 35, 38, 43, 48].

A final remark regarding the scaling and design of experiments for oscillating AF investigations: in general, there are four independent parameters defining the problem (see also [64], as well as [65]). We are used to working with the following dimensionless quantities, containing only known parameters:

- the flapping $\mathrm{Re}_{\mathrm{vmax}} = (v_{\max} R/v)$,
- a velocity ratio, say $(v_\infty/v_{\max})$,
- the frequency of oscillation $\mathrm{Str}_\infty = (f_{\mathrm{OS}}\,\mathrm{R}/v_\infty)$,
- the amplitude $A_{\mathrm{A}} = (s_{\mathrm{o}}/\mathrm{R})$ or φ_{o}.

The author prefers, however, to use the following alternatives, in order to avoid degenerations in the case of $v_\infty = 0$ and to simulate physics more correctly by accounting for the fact that the mean through-flow velocity v_{m} always stays $v_{\mathrm{m}} > v_\infty$, and it never vanishes. The v_{m} through the AF has two independent components, the free-stream and the 'self-pumping' velocity:

- $\mathrm{Re}_{\mathrm{vmax}} = (v_{\max} R/v)$,
- $f = (v_{\mathrm{m}}/v_{\max})$,
- $\mathrm{Str}_{\mathrm{m}} = (f_{\mathrm{OS}} R/v_{\mathrm{m}})$,
- $A_{\mathrm{A}} = (s_{\mathrm{o}}/R)$ or φ_{o}.

These parameters produce more meaningful results for oscillating AFs. The a priori unknown v_{m} is approximated by $v_{\mathrm{m}} = v_\infty + C_{\mathrm{m}}\, v_{\mathrm{id}}$. The mean induced jet velocity v_{id} is determined iteratively [C_{m} is an empirical factor, see eqn (11)].

5 Vortex methods and the FVM

Vortex-based simulation models differ vastly: they may use large, specific types of vortices to calculate forces [18], or they may come up with CFD methods, employing small, discrete vortex filaments to simulate a flow field [19]. Recent developments of LES are able to numerically follow large, real vortices in space and time [20].

Rayner introduced his 'ring vortex model' in 1979 [18], which makes use of the vortices emanating from the wing tips of birds (tip vortex (TV) [15]). He claims, that the TVs form time-dependent ring vortices that detach from the flapping wings. Phenomenologically this turns out to be quite realistic for some birds and low flight velocities. Unfortunately, calculated ring vortex forces F_{L} are too small to carry the weight of other birds at higher velocities (see the discussion of Hedenström [10] and Spedding [44]. In addition, we have to keep in mind that nature as well as aircraft designers always want to minimize the parasitic TVs, in order to keep the induced drag as low as possible [3].

Recently, a number of advanced vortex methods were published [20]. Here, free, discrete vortex elements are utilized to model a flow field; their interaction is expressed following the law of Biot–Savart. The grid-free Lagrangian LES methods are very general: unsteady, low and high Re number flows plus heat transfer can be treated. Also a group of steady and unsteady vortex-lattice methods should be mentioned [19, 42]. Some of those have been successfully applied to animal propulsion.

Another group of methods uses ‘first aerodynamic principles’, employing explicit equations for solution. Zbikowski [21] developed such a modular approach; his current version has been applied to laminar, inviscid flow situations [66].

Generally speaking, there is a lack of physical understanding of flow phenomena occurring in unsteady, viscous flow situations. Classical models and tools are not applicable. Specialized NS simulations are the only means for analysis. However, they do need information on turbulence modeling, near-wall flow structure, etc., and they are costly. It is surprising to the author that unsteady flow analyses (Birnbaum *et al.*, 1920) and vortex methods over the last 90 years all maintain the classic ‘smooth flow condition’ (Kutta–Joukowski), at the trailing edge of an AF though it is generally accepted for quite some time that a ‘smooth flow’ is physically unrealistic under unsteady flow conditions with $f \leq$ ca. 5–10, $\mathrm{Str}_\infty \geq$ ca. 0.20.

5.1 Finite vortex modeling

In the early days (1938), during in-flight flow visualizations on the fast fighter Me-109 and other aircraft, W. Liebe went a step back to improve the physical understanding of both the generation and the breakdown of lift (see later publications and [67]). He replaced the mathematical relation of Kutta–Joukowski by a more general physical condition at the trailing edge of a fixed AF, illustrated in Fig. 11A. The sketch shows that allowing for a normal flow around the trailing edge, leads to a periodic, unsteady roll-up of a so called ‘TEV’ (high frequency, small trailing edge vortices). Furthermore, it can be shown that the self-sustained, intermittent suction S (on the right side of the RSP) during the four subsequent stages $t_1 < t_2 < t_3 < t_4$ is able to maintain an average, approximate ‘smooth flow condition’ at the trailing edge (see Section 7) [22]. This, together with studies on unsteady aerodynamics in nature, was the first step of W. Liebe towards his ‘finite vortex model’, formulated in 1963 [2].

The next two sections describe the physical justification of this concept and the dynamic vortex simulation, which is particularly suited to describe the performance of oscillating AFs. Figures 9–12 are used to illustrate the basic FVM as well as later extensions.

It is historically interesting to note how long it took—in spite of the advent of modern experimental and numerical tools—to confirm earlier physical hypotheses and to improve current understanding. Nowadays, advanced experimental techniques allow to survey and visualize 2D or 3D unsteady flow fields: LDA (laser doppler anemometry), Schlieren photography, light sheet technique, DPIV (digital particle image velocimetry), H_2 bubble tracing, and vortex tagging with smoke, $TiCl_4$ or colored liquids.

In spite of this, it is still difficult to identify and interpret small (though strong), embedded vortices like the TEV (see the experience of Spedding [44] and Kompenhans [68]). Figure 12 shows smoke visualizations of both TEV and BV, LEV formation around a pitching AF. Panda and Zaman [43] clearly demonstrate the importance of how/where to position the tagging smoke wire. In addition to this, specific know-how is required [44] to process/evaluate experimental data (DPIV, LDA), in order to clearly identify mathematically the TEV in the near-field of an AF. Nevertheless, up to now a large number of experiments have accumulated proof of the existence of both the small but strong TEV and the dynamic stall vortex or LEV as part of the BV (see [8, 10, 35, 38, 41, 43, 44, 51] and also [69] and [70]).

The numerous oscillating AF experiments have been paralleled by many NS investigations, recently extended to the analysis of swimming fish as well as flying insects and birds. To mention some of them: Gustafson [9, 63], Mehta [31], Ke-Qin [58], Sun [50], Ramamurti [62], Zheng [47] and Thiele [30].

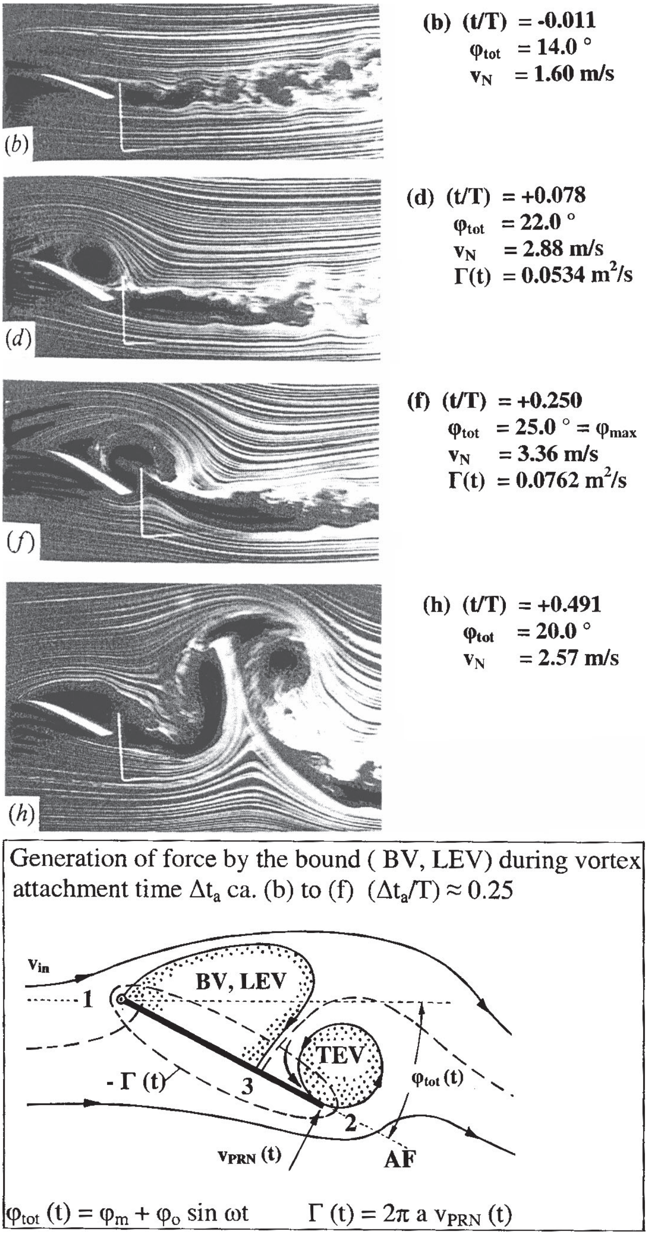

Figure 9: Formation of a vortex pair TEV/BV, LEV around a pitching AF with $\mathrm{Re_R} > \mathrm{Re_{vmax}} >$ 20 K during the down motion over appoximately half a cycle: $(t/T) = 0$–0.50. Top left: Pure pitching experiment in air, NACA 0012, with $\mathrm{Re_R} = 44$ K, $\mathrm{Re_{vmax}} = 21.7$ K, $\mathrm{Str}_\infty = 0.0637$, $\varphi_m = 15°$, $\varphi_o = 10°$, $f_{OS} = 4.25$ Hz; smoke visualizations of (b) (d) (f) and (h) taken from fig. 2 in [43]. Top right: Phase data for (b) (d) (f) and (h) with time (t/T), φ_{total} and $v_N(t)$ at the trailing edge. Bottom: Sketch of typical system of counterrotating vortices TEV and BV, LEV with the TEV and $v_{PRN}(t)$ being the prime driver.

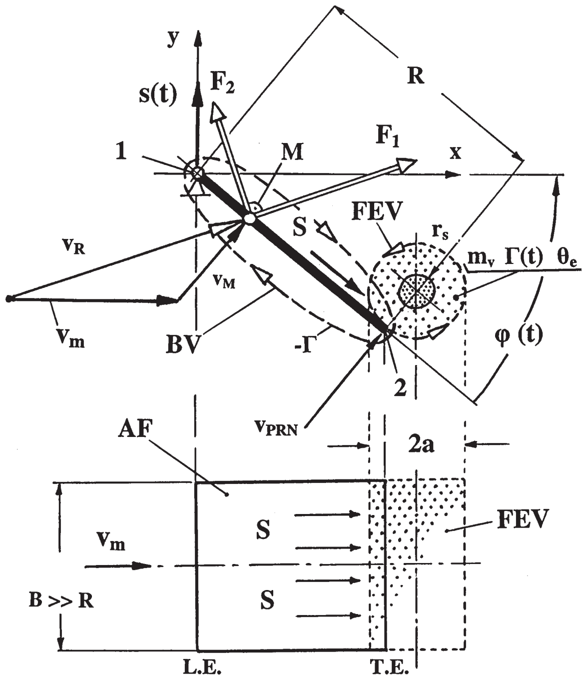

Figure 10: Concept of the extended finite vortex model (1): 2D kinematics imposed on a flat plate. The $-\varphi(t)$, $-s(t)$ down motion of the trailing edge (TE) and the mean flow-through velocity v_{m} from the left side lead to the roll-up of the TEV (FEV). The resulting suction S (left from the RSP) with its equivalent counterrotating BV is shown in a simplified manner [4]. The BV is assumed to attain $-\Gamma$, compensating the TEV with its $+\Gamma$.

Figure 9 depicts smoke visualizations of a TEV/BV, LEV formation process during the down motion of an oscillating AF over $\approx T/2$ [43]. A sketch simplifies the TEV/BV, LEV interplay during the vortex residence time Δt_{a}. This is used in Fig. 10 to demonstrate the concept of the extended FVM. Figure 10 indicates a down motion snapshot of the 2D oscillation $(-\varphi(t) - s(t))$ of a flat plate with an arbitrary flow-through velocity v_{m}. The TEV is modeled by a finite, natural vortex [3], the radius of which is limited to a finite value $r \leq a$. Also indicated is the suction S, as a result of the spinning finite edge vortex (FEV = TEV). This counterclockwise TEV has a finite mass $m_{\mathrm{v}} = (\pi a^2 B \rho)$, a circulation $\Gamma(t) = 2\pi a v_{\mathrm{PRN}}(t)$ and an equivalent moment of inertia Θ_{e}. The TEV itself is generated by the net normal velocity component $v_{\mathrm{PRN}}(t)$ around the trailing edge. Compatibility, or ‘no slip’ requires that the vortex peripheral velocity always equals the normal flow $(a\,\mathrm{d}\O(t)/\mathrm{d}t) = \mathrm{v}_{\mathrm{PRN}}(t)$ (see Fig. 14 for more details). For simplicity, Fig. 10 does not show an LEV which may be formed as part of the BV. The suction S with its near-wall flow velocity (see the ‘Mantelströmung’ [71]) can be visualized as a clockwise, compensating vortex around the AF, which is always present. As a bound vortex (on the left side of the RSP) it is named BV, and it has the opposite/equal circulation—$\Gamma(t)$, so that Thomson’s law is satisfied: $\sum(+\Gamma - \Gamma) = 0$. As part of the extended FVM [4], Fig. 10 also shows the velocity triangle with the resultant vector $v_{\mathrm{R}}(t) = v_{\mathrm{M}}(t) + v_{\mathrm{m}}$ at the moment-free quarter chord reference point M. Finally, considering the ‘unsteady Magnus effect’ [13], the aerodynamic interaction between

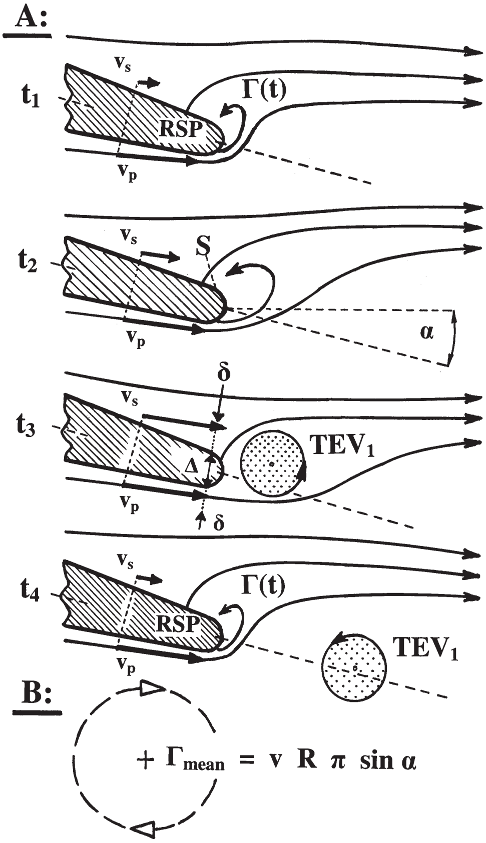

Figure 11: The fixed, inclined AF: How to physically maintain the Kutta–Joukowski condition during flight? (A) Enlarged vicinity of the sharp trailing edge (AF chord R, trailing edge thickness Δ), depicting the intermittent suction mechanism in four stages: t_1, roll-up of the TEV_1 starting at $v_\mathrm{p} > v_\mathrm{s}$; build-up of a suction S [equivalent bound countercirculation $-\Gamma(t) = -2\pi\, a v_\mathrm{PRN}\,(t)$]; t_2, increasing size/rotation/suction of the TEV_1; the RSP is moving towards the trailing edge; t_3, intermittent satisfaction of the 'Kutta/smooth flow condition' with $v_\mathrm{p} = v_\mathrm{s}$; full vortex size $(2a/R)$ reached; hypothesis: $(2a/R)$ is typically limited by $(\Delta + 2\delta)/R \approx 0.02$–$0.10$ for fixed AFs; t_4, high frequency shedding of the TEV_1; the RSP is jumping back upstream a TEV_2 is rolled-up, etc. Cycle time: $T = (t_4 - t_1)$. (B) Current view [15]: application of the mathematical condition of Kutta–Joukowski, requiring a circulation $\Gamma_\mathrm{mean} = vR\pi \sin\alpha$.

$v_R(t)$ and the $-\Gamma(t)$ of the BV generates the 'Magnus force' $F_2(t)$. The orthogonal drag force $F_1(t)$ is due to the AF skin friction only.

After discussing the physical background and the modeling concept, we give a chronological sequence of eight phases, characterizing and summarizing oscillating AF dynamics with the mechanisms proposed within the extended FVM (Figs 10 and 11):

1. Viscous forces and radial balance between centrifugal and pressure forces lead to the 'curved' flow with a normal component v_N and a TEV roll-up. This unsteady edge flow mechanism

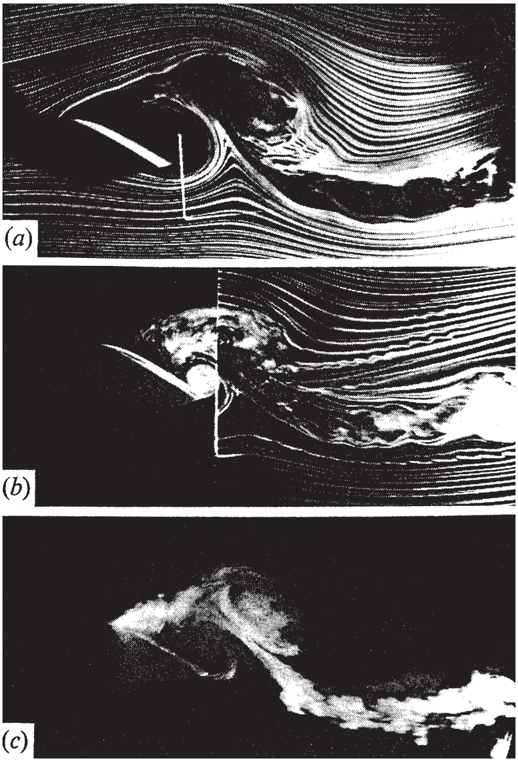

Figure 12: Smoke visualization of unsteady formation of the TEV and (BV, LEV) from a pitching AF in air, $\mathrm{Re}_\mathrm{R} = 22\,\mathrm{K}$, $\mathrm{Str}_\infty = 0.0637$, $\varphi_\mathrm{m} = 15°$, $\varphi_\mathrm{o} = 10°$, $f_\mathrm{OS} = 2.13\,\mathrm{Hz}$, NACA 0012, taken from [43]. Visibility of the TEV and LEV strongly depends on the positioning of the smoke wire: (a) at the upstream leading edge: the TEV/LEV is visible; (b) at the downstream trailing edge: the TEV is visible; (c) smoke wire at the lower AF side: the TEV/LEV is visible.

plays a key role. There is no 'smooth flow condition', and the RSP swings to the suction side of the trailing edge (Fig. 11).

2. The TEV, as a real edge vortex, is simulated by a natural vortex, defined in [3]; it has

   - two flow regimes: the inner 'solid core' (rot $v \neq 0$) and the outer potential flow ($r \to \infty$);
   - a nonzero viscosity and density;
   - three drivers for vortex roll-up: the normal velocity $v_\mathrm{PRN}(t)$, the radial force balance and a finite viscosity.

3. Start and termination of a net TEV: when v_PRN is prevailing over v_m (see down phase Fig. 10), the following equations determine start/termination for a purely pitching AF:

$$
\begin{aligned}
t_\mathrm{start}\ \text{from}\quad \cos\omega t &= -f\sin\varphi, && (1)\\
t_\mathrm{end}\ \text{from}\quad \sin\omega t &= f\,\varphi_\mathrm{o}\cos\varphi\cos\omega t.
\end{aligned}
$$

Within $\Delta t_\mathrm{a} = (t_\mathrm{end} - t_\mathrm{start})$ we get a net, active counterclockwise rotating, luff-side TEV that stays attached to the trailing edge. It is found from experiments that the vortex attachment to the AF is terminated when $v_{\mathrm{PRN}}(t)$ reaches its maximum, given by $\mathrm{d}v_{\mathrm{PRN}}/\mathrm{d}t = 0$. It is also found that $\Delta t_{\mathrm{a}} \approx T/4$.

4. The TEV growth is controlled/limited primarily by $v_{\mathrm{PRN}}(t)$. Within a very short time $(\Delta t_{\mathrm{f}}/\Delta t_{\mathrm{a}}) \ll 1.0$, the TEV radius grows to a stable level $r = a$ [finite vortex diameter $(2a/R)$]. The parameter $(2a/R)$ plays a key role in the overall dynamic vortex–structure interaction. Its value, however, is a priori unknown. There are two phases of TEV growth, always satisfying the 'no-slip' condition $(r\,\mathrm{d}\emptyset/\mathrm{d}t) = v_{\mathrm{PRN}}$). The 'feeding': r rises to $r = a$. The 'rotational acceleration': Γ finally rises to its maximum $\Gamma_{\max} = 2\pi a \max v_{\mathrm{PRN}}$.
5. At maximum suction/near-wall velocity with $\max \Gamma = 2\pi a \max v_{\mathrm{PRN}}$, the RSP moves from the suction side downstream close to the trailing edge. Now temporarily a 'smooth flow condition' is reached (fixed AF example in Fig. 11). The mean circulation over one cycle T is:

$$\Gamma_{\mathrm{mT}} = -(1/\pi)\Gamma_{\max} = -2a \max v_{\mathrm{PRN}}. \tag{2}$$

6. During the 'active phase' $0 < t < \Delta t_{\mathrm{a}}$ the TEV-triggered suction S—on the right side of the RSP—is taken care of by an equivalent BV—on the left side of the RSP (Fig. 10). According to Thomson's law, the BV counter circulation must be $-\Gamma(t) = -2\,\pi a v_{\mathrm{PRN}}(t)$.
7. Next it is proposed that a circulatory force $F_2(t)$ is generated by the aerodynamic, instantaneous interaction between the resultant velocity vector $v_{\mathrm{R}}(t)$ and the rotation $-\Gamma(t)$ of the BV:

$$F_2(t) = -\Gamma(t)\,\rho B\, v_{\mathrm{R}}(t). \tag{3}$$

It is also proposed to include the profile wall friction $F_1(t)$ by using the dynamic profile quality $\zeta_{\mathrm{dyn}}\,(\alpha_{\mathrm{dyn}})$, taken from dynamic experiments on that AF (see Fig. 2 and [40]):

$$F_1(t) = F_2(t)/\zeta_{\mathrm{dyn}}\,(\alpha_{\mathrm{dyn}}). \tag{4}$$

8. After Δt_{a} the overall velocity and static pressure field cannot further keep the TEV attached, it detaches from the trailing edge into the wake. Force production is assummed to terminate at that instant.

5.2 Extensions and modifications of the FVM

Table 1 compares the basic FVM proposed by W. Liebe [2, 22, 71] with the current extended/ modified FVM proposed by R. Liebe, [4–7].

In the meantime, several comparative FVM calculations have been done: both using different FVM formulations (see also the approximations in Section 6.5 as well as [3]) and analyzing published experiments on oscillating AFs including force and circulation measurements, [2, 8, 9, 35, 38]. The following FVM lessons can be summarized to date for oscillating AFs:

- Qualitative agreement was generally reached when analyzing experiments with the basic and the extended FVM as well as FVM approximations.
- Satisfactory and consistent quantitative agreement was obtained with the extended FVM only. The basic FVM generally overestimates the forces generated.
- When using the preliminary relation for the vortex size $(2a/R)$—Fig. 15—the extended FVM yields forces, circulations, etc., within approximately ±20%.
- More work is needed on the key parameter $(2a/R)$.

Table 1: The FVM: 1963–2005.

Subject	Basic model (1963)	Extended model (2005)
1. The Kutta–Joukowski condition and the TEV	• The 'edge flow mechanism' feeds and spins a TEV attached to the trailing edge. The normal v_{N} is the driver.	• Same
	• Replacement of the Kutta condition by a more general condition: $v_{\mathrm{PRN}}(t) \neq 0$.	• Same
2. Dynamic TEV/AF interaction	• Rapid formation of a finite, stable TEV with $(2a/R)$ and m_{V}	• Same
	• Acceleration of the finite mass m_{V} by the prescribed AF kinematics. At the time Δt_a, the m_{V} detaches radially from centrifugal action.	• Translation and rotation of the vortex are obtained from the coupled, dynamic TEV/AF interaction—eqn (7). Both m_{V} and θ_{e} are entered the analysis. m_{V} detaches tangentially.
	• Replacement of the Kutta condition by a more general condition: $v_{\mathrm{PRN}}(t) \neq 0$.	• Same
3. Starting, residence/attachment time Δt_{a}	• v_{PRN} and the TEV increase from $t = t_{\mathrm{start}} = 0$ to $t = t_{\mathrm{end}} = T/4$, reaching max v_{PRN} at $\mathrm{d}^2\varphi/\mathrm{d}t^2 = 0$.	• A 'net TEV' is defined = the difference between a thrust-type vortex on the luff side of the AF and a drag-type vortex on the lee side. This causes a delay of $t_{\mathrm{start}} > 0$ and $t_{\mathrm{end}} > T/4$. $\Delta t_{\mathrm{a}} \approx T/4$.
4. The size $(2a/R)$ of the TEV for oscillating and fixed AFs	• For oscillating and fixed AFs the TEV size is believed to be constant, i.e. $(2a/R) =$ 0.30–0.35.	• $(2a/R)$ is found to vary in a characteristic range. Up-to-date analyses of experiments show the preliminary relation of Fig. 15. *Oscillating AF* Experiments [2]: $(2a/R) =$ 0.27–0.67 Nature: $(2a/R) \approx$ 0.4–0.6 *Fixed AF (engineering)* $(2a/R) \approx$ 0.03–0.15
Effects of the free-stream velocity v_∞	• Free-stream v_∞ effects are not considered (still fluid).	• v_∞ effects plus a near-field velocity v_{m} are considered.
5. Inertial and circulatory loads from fluid dynamics	• Consideration of translatory inertial forces from the TEV mass m_{V} only	• Translatory and rotational inertial loads taken care of. The structure of the natural

Table 1: *Continued*

Subject	Basic model (1963)	Extended model (2005)
	• 'Mantelströmung' postulated, but no circulatory loads considered	vortex (solid core, outer potential) is taken care of (θ_e). • 'Unsteady Magnus effect' used to calculate the circulatory forces $F_2(t)$ from the $-\Gamma(t)$ and the $v_R(t)$. The drag force $F_1(t)$ is obtained via the dynamic profile quality ζ_{dyn}.

First attempts to apply the FVM to fixed AFS (i.e. airplane wings), have been encouraging (see Section 7) [6]. The approximate eqn (14) is employed as a starting point, and the following dimensionless relations can be derived for the force coefficients C_T and C_L, respectively:

$$\text{Oscillating AF:} \quad \begin{pmatrix}\text{Detaching vortex}\\ \text{frequency}\end{pmatrix}^2 (\text{AF amplitude}) \begin{pmatrix}\text{Vortex size}\\ 2a/R\end{pmatrix}^4 = C_T\,(\text{Thrust force}). \tag{5}$$

$$\text{Fixed AF:} \quad \begin{pmatrix}\text{Shedding vortex}\\ \text{frequency}\end{pmatrix} \begin{pmatrix}\text{AF angle of attack,}\\ \text{trailing edge thickness}\end{pmatrix} \begin{pmatrix}\text{Vortex size}\\ 2a\,/R\end{pmatrix}^2 = C_L\,(\text{Lift force}). \tag{6}$$

It is too early to draw general conclusions from the FVM applications to fixed AFs.

5.3 How to control the TEV/BV, LEV?

After discussing the TEV/BV formation, the TEV interaction with the (BV, LEV) and the force-enhancing stabilization of the (BV, LEV) system, we summarize how to control the TEV/BV, LEV. The following findings for three Str_∞ ranges are extracted from Zaman's visualization experiments [43] for oscillating AFs:

- Small $\mathrm{Str}_\infty \leq 0.03$
  - — no visible unsteady effects;
  - — no pairs TEV/BV, LEV detectable;
  - — circulatory forces dominate over inertial ones;
  - — classical aerodynamics methods are applicable.
- Medium $\mathrm{Str}_\infty = 0.06$–$0.25$
  - — unsteady flow;
  - — TEV and an LEV (as part of a BV) are visible;
  - — detachment of the TEV and the LEV at about the same time $(\Delta t_a/T) \approx 0.25$;
  - — TEV–LEV interaction continues after detachment: formation of upside mushroom-like structures (Fig. 9);
  - — only specialized, large-scale, unsteady NS simulations are applicable.

- Large $\mathrm{Str}_{\infty} = 0.25$–$0.50$
  - — the unsteadiness and the TEV are stronger;
  - — the LEV(as part of a BV) is clearly stabilized by the TEV: protection from fluid in-rush into the LEV core (with potential vortex/force breakdown);
  - — extended residence time of the (BV, LEV) system: $(\Delta t_{\mathrm{a}}/T) \approx 0.50$; enhanced mean F_2;
  - — higher Str_{∞}: two LEVs forming on the suction side simultaneously (a strong LEV_1 detaching from the trailing edge, a weaker LEV_2 forming at the leading edge);
  - — after detachment: formation of inverted mushroom-like structures; increased spacing of vortex pairs in the wake: 1.5–2 rising to ≥ 10 chords;
  - — inertial forces dominate over circulatory ones;
  - — only specialized, large-scale, unsteady NS simulations are applicable.

From today's experience the author believes that the described vortex interaction for fixed AFs can be beneficially controlled by:

1. tripping edges along the leading edge, turbulence or vortex generators [49];
2. slotted flaps and slats [15], splitter plates;
3. periodic blowing and suction, static blowing [30, 36, 47];
4. fences or BL fences [22];
5. self-actuating flaps (backflow barriers) (see Fig. 20 and [25–28, 72]).

Currently, there is little known on the quantitative effectiveness of items 1–5 for oscillating AF-vortex control [42, 45]; more work is needed.

6 The FVM for oscillating AFs

The assumptions and modeling concepts outlined (Figs 10 and 14) are used to derive the mechanical relations describing the coupled vortex/AF/support/free-stream flow dynamics [73]. From the following general equations, further specific cases and approximations are derived.

6.1 General equations of motion and solution strategies

The following table summarizes the general equations of motion, which describe the vortex–structure interaction dynamics, [4, 23]:

---

1. Equilibrium (D'Alembert–Lagrange, discrete explicit equations):
   $\sum_i (F_x - m_{\mathrm{v}} \mathrm{d}^2 x_{\mathrm{s}}/\mathrm{d}t^2)_i = 0 \quad \sum_i (F_y - m_{\mathrm{v}} \mathrm{d}^2 y_{\mathrm{s}}/\mathrm{d}t^2)_i = 0 \ \sum_j (M - \theta_{\mathrm{e}} \mathrm{d}^2 \O/\mathrm{d}t^2)_j = 0$
2. Kinematics (explicit equations):
   $\varphi(t)\, \mathrm{d}\varphi/\mathrm{d}t\, \mathrm{d}^2\varphi/\mathrm{d}t^2$ and $s(t)\, \mathrm{d}s/\mathrm{d}t\, \mathrm{d}^2 s/\mathrm{d}t^2$ as functions of time t
3. Compatibilities (explicit equations):
   $v_{\mathrm{PRN}}(t) = \pm a \mathrm{d}\O(t)/\mathrm{d}t \quad \mathrm{F}_2(t) = \Gamma(t)\rho B v_{\mathrm{R}}(t) \quad F_1(t) = F_2(t)/\zeta_{\mathrm{dyn}}(\alpha_{\mathrm{dyn}})$
   with $\Gamma(t) = 2\pi a v_{\mathrm{PRN}}(t) \quad \theta_{\mathrm{e}} = f_{\mathrm{D}}(n) m_{\mathrm{v}} a^2/2 \quad m_{\mathrm{v}} = \pi a^2 \rho B\, n = (a/r_{\mathrm{s}})$
4. Motion, forces, moments, powers (integration in time):
   $x_{\mathrm{s}}\, \mathrm{d}x_{\mathrm{s}}/\mathrm{d}t\, \mathrm{d}^2 x_{\mathrm{s}}/\mathrm{d}^2 t; \quad y_{\mathrm{s}}\, \mathrm{d}y_{\mathrm{s}}/\mathrm{d}t\, \mathrm{d}^2 y_{\mathrm{s}}/\mathrm{d}^2 t; \mathrm{d}^2\O/\mathrm{d}t^2 =$
   $f(t, \text{geometry}, \varphi_{\mathrm{o}}, s_{\mathrm{o}}, \omega, \psi, a, f)$ (7)

$\mathrm{H}_i\mathrm{V}_i$; $\mathrm{H}_z\mathrm{V}_z$ and $\mathrm{M}_i\mathrm{M}_z$ also $= f(t, \text{geometry}, \varphi_\mathrm{o}, s_\mathrm{o}, \omega, \psi, a, f)$
$\mathrm{H}(t) = \mathrm{H}_i + \mathrm{H}_z$ $\mathrm{V}(t) = \mathrm{V}_i + \mathrm{V}_z$ and $\mathrm{P}t = \mathrm{M}(t)\mathrm{d}\varphi(t)/\mathrm{d}t = \mathrm{P}_i + \mathrm{P}_z + \mathrm{P}_B$
with $\mathrm{M}(t) = \mathrm{M}_B + \mathrm{M}_i + \mathrm{M}_z$ $\mathrm{M}_B = -\theta_\mathrm{e}\mathrm{d}^2\text{Ø}/\mathrm{d}t^2$

5. Solution strategy:
   (i) Supported AF: Mean reaction forces (over T): $H_\mathrm{mT} = 1/T\int_0^T H(t)\mathrm{d}t$
   Mean power required: $\mathrm{P}_\mathrm{mT} = 1/T\int_0^T P(t)\mathrm{d}t$, *etc.*
   (ii) Freely moving AF: with 'swimming velocity' v_s, reaction force = external drag
   $\mathrm{H}_\mathrm{mT} = \mathrm{F}_\mathrm{D,ext} = f(\mathrm{Re}, v_\mathrm{s}, \text{geometry}, \varphi_\mathrm{o}, s_\mathrm{o}, \omega, \psi, a, f)$ Iteration for v_s

The computer code 'fvm-1' (pitching/plunging AFs, 4/2002) solves iteratively by simultaneous time integration of the above four blocks 1–4 [4, 23]. Main results are time-dependent forces/moments/circulation and power requirements. For clarity, most analyses are done for zero structural mass ($m_\mathrm{s} = 0$) in order to show the genuine fluid effects ($m_\mathrm{v} \neq 0$). There are two possible solution strategies for iteration:

(i) Supported/guided AF: It requires a 'once through integration' for one fixed set of unknowns. In some cases iteration is done via f to satisfy $\mathrm{H}_\mathrm{mT}|_\text{measured} = \mathrm{H}_\mathrm{mT}|_\text{fvm - calculated}$ (see Figs 13 and 17).
(ii) Freely moving AF: It requires a searching approach to arrive at a consistent set of all unknowns, including say a swimming (v_s) or flying (v_F) velocity. Then side conditions are: mean thrust = mean body drag, and/or mean lift = total body weight [45].

6.2 Equations of motion for pure pitching

For a purely pitching AF, the following specific equations are derived from eqn (7), when, for clarity, only the fluid mass $m_\mathrm{v} \neq 0 (m_\mathrm{s} = 0)$ is considered:

- Prescribed, pure harmonic pitching is

$$\varphi(t) = \varphi_\mathrm{m} + \varphi_\mathrm{o}\sin\omega t \; \mathrm{d}\varphi(t)/\mathrm{d}t = \varphi_\mathrm{o}\,\omega\cos\omega t \; \mathrm{d}^2\varphi(t)/\mathrm{d}t^2 = -\varphi_\mathrm{o}\omega^2\sin\omega t,$$

  with the velocity triangles in Figs 10 and 14 the driving component $v_\mathrm{PRN}(t)$ and at the quarter chord point M the $v_\mathrm{R}(t)$ become with the abbreviation $v_\mathrm{max} = (\varphi_\mathrm{o}\,\omega\, R_\mathrm{eff})$:

$$v_\mathrm{PRN}(t) = v_\mathrm{max}(\cos\omega t + f\,\sin\varphi), \tag{8}$$
$$v_\mathrm{R}(t) = v_\mathrm{max}/4[16f^2 + \cos^2\omega t + 8f\cos\omega t\sin\varphi]^{1/2}.$$

- The circulatory interaction force $F_2(t)$ and, via the dynamic profile quality ζ_dyn, also $F_1(t)$ become:

$$F_2(t) = \Gamma(t)\rho B v_\mathrm{R}(t) = 2\pi a\rho B v_\mathrm{PRN}(t) v_\mathrm{R}(t) \quad F_1(t) = F_2(t)/\zeta_\mathrm{dyn}(\alpha_\mathrm{dyn}), \tag{9}$$

  with their directional angles $\alpha_\mathrm{M}(t) \leftrightarrow \alpha_x$ and $\gamma_\mathrm{M}(t)$ as well as the Ø derivative:

$$\alpha_\mathrm{M}(t) = \arctan\left[(¼\,1/f\cos\omega t + \sin\varphi)/\cos\varphi\right] \quad \text{and} \quad \gamma_\mathrm{M}(t) = \pi/2 + \varphi(t) - \alpha_\mathrm{M}(t)$$
$$\mathrm{d}^2\text{Ø}/\mathrm{d}t^2 = -v_\mathrm{max}\omega/a[-\sin\omega t + f\varphi_\mathrm{o}\cos\varphi\cos\omega t].$$

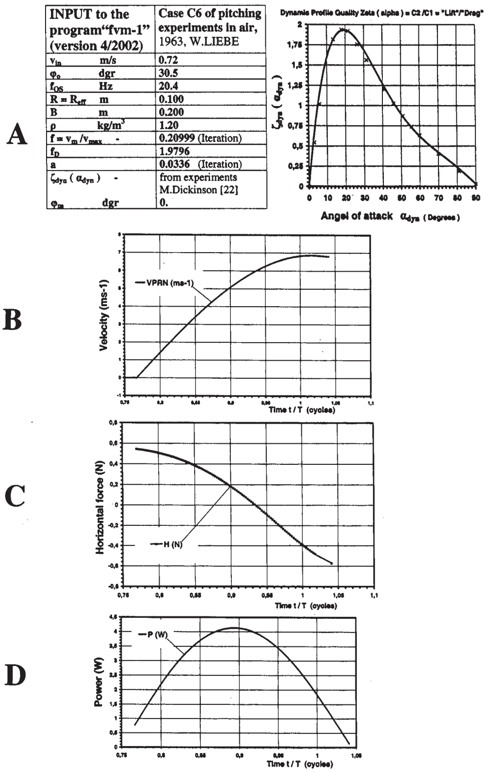

INPUT to the program"fvm-1" (version 4/2002)		Case C6 of pitching experiments in air, 1963, W.LIEBE
v_{in}	m/s	0.72
φ_o	dgr	30.5
f_{OS}	Hz	20.4
$R = R_{eff}$	m	0.100
B	m	0.200
ρ	kg/m^3	1.20
$f = v_m / v_{max}$	-	0.20999 (Iteration)
f_D		1.9796
a		0.0336 (Iteration)
$\zeta_{dyn}(\alpha_{dyn})$	-	from experiments M.Dickinson [22]
φ_m	dgr	0.

Figure 13: FVM results (1): Typical time-dependent quantities over the approximate quarter cycle (upstroke): normal velocity v_{PRN}, horizontal force H and power requirements P from an 'fvm-1' analysis of a single pitching AF experiment C6 in air [2]. (A) Input to the program 'fvm-1' (2002); (B) normal velocity $v_{\mathrm{PRN}}(t/T)$ of the trailing edge; (C) horizontal net thrust force $H(t/T)$; mean force over T; $H_{\mathrm{mT}} = +0.07483$ N; (D) power $P(t/T)$ required to maintain the prescribed kinematics with pure pitching $\phi(t) = \varphi_{\mathrm{o}} \sin \omega t$; mean power over T: $P_{\mathrm{mT}} = 1.508$ W. see also Fig. 17.

- The inertial and circulatory force contributions are as follows:

$$\begin{aligned}
&\mathrm{H}_i(\text{or } V_i) = m_{\mathrm{v}} \mathrm{d}^2 x_{\mathrm{s}}/\mathrm{d}t^2 \,(\text{or } m_{\mathrm{v}} \mathrm{d}^2 y_{\mathrm{s}}/\mathrm{d}t^2) && \text{and} \\
&H_z = (F_2 \cos \gamma_{\mathrm{M}} - F_1 \sin \gamma_{\mathrm{M}}) && V_z = (F_2 \sin \gamma_{\mathrm{M}} + F_1 \cos \gamma_{\mathrm{M}}) \qquad (10) \\
&M_i = m_{\mathrm{v}}(-\mathrm{d}^2 x_{\mathrm{s}}/\mathrm{d}t^2 y_{\mathrm{s}} + \mathrm{d}^2 y_{\mathrm{s}}/\mathrm{d}t^2 x_{\mathrm{s}}) && \mathrm{M}_z = \mathrm{R}_{\mathrm{eff}}/4[-\mathrm{H}_z \sin \varphi + \mathrm{V}_z \cos \varphi].
\end{aligned}$$

- The induced, mean velocity level v_{id} taking a constant v_{id}, across an approximate jet cross section A_{ka}, is obtained from the mean mass flow $m = m_{\mathrm{v}}/T = \rho a^2 B \omega$ as follows:

$$v_{\mathrm{id}} = (2a/R)^2 B R^2 \omega/(4A_{\mathrm{ka}}) \quad \text{with} \quad A_{\mathrm{ka}} = RB\,[(2a/R)\cos \varphi_{\mathrm{o}} + 2(R_{\mathrm{eff}}/R)\sin \varphi_{\mathrm{o}}]\,.$$

The actual duration of the attachment phase is $(t_{\mathrm{end}} - t_{\mathrm{start}}) = \Delta t_{\mathrm{a}}$. By the superposition of both the 'active' (thrust) and 'passive' (drag) vortices, one can explicitly determine the Start (t_{start}) and the End (t_{end}). These times bracket the active attachment phase for numerical integration of the equations of motion. The following transcendental equations (see Figs 10 and 14) are used to quantify $\Delta t_{\mathrm{a}} = (t_{\mathrm{end}} - t_{\mathrm{start}})$:

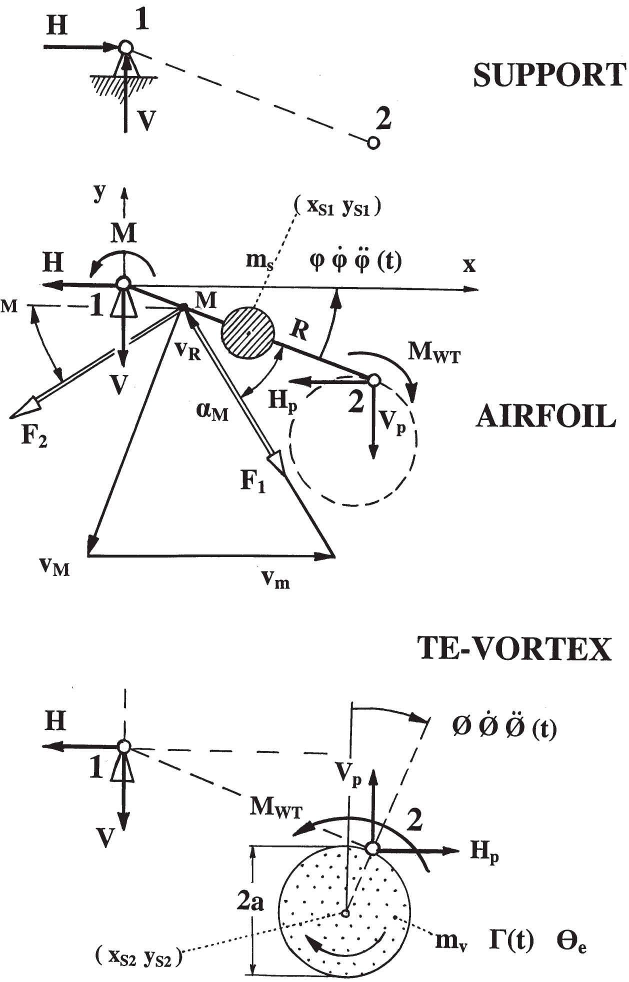

Figure 14: Concept of the extended finite vortex model (2): Pure pitching of an AF, pivoted around its supported leading edge '1'. Time dependent quantities (deformations, external/internal loads etc. for the coupled dynamics of the finite TEV, the airfoil and its support. See eqns (7–11) and also [4, 5].

- Start: $\cos \omega t = -f \sin \varphi$ 'zero velocity' yields t_{start} (zero v_{PRN}),
  End: $\sin \omega t = f \varphi_0 \cos \varphi \cos \omega t$ 'maximum velocity' yields t_{end}(peak v_{PRN}).
- Finally it should be mentioned that experimental findings from [35] on the near-field axial velocity distribution are used to improve the 'self-pumping' velocity distribution v_{m} along the AF as follows:

$$\begin{array}{ll} \text{instead of} & C_{\text{in}} = 0 \;\; C_{\text{m}} = 0.50 \;\; C_{\text{out}} = 1.0 \\ \text{in} & v_{\text{in}} = v_\infty + C_{\text{in}} v_{\text{id}} \;\; v_{\text{m}} = v_\infty + C_{\text{m}}\, v_{\text{id}} \\ & v_{\text{out}} = v_\infty + C_{\text{out}}\, v_{\text{id}} \\ \text{we use the improvements} & C_{\text{in}} = 0.7095 \;\; C_{\text{m}} = 0.7821 \;\; C_{\text{out}} = 1.0. \end{array} \qquad (11)$$

6.3 Typical results

Figure 13 shows typical FVM results from analyzing the pitching-AF single test case C6 of approximately 40 experiments in air [2] (see also Fig. 17).

'fvm-1'-Input

In-flow velocity	$v_{\mathrm{in}} = 0.72\,\mathrm{m/s}$	Air density	$\rho = 1.20\,\mathrm{kg/m^3}$
Pitching amplitude	$\varphi_{\mathrm{o}} = 30.5$ degree	Kinematic viscosity	$\nu = 15.1 \times 10^{-6}\,\mathrm{m^2/s}$
Pitching frequency	$f_{\mathrm{OS}} = 20.4\,\mathrm{Hz}$		
AF (plate) chord	$R = 0.10\,\mathrm{m}$	Velocity ratio	$f = 0.20999$
Pitching lever	$\mathrm{R_{eff}} = 0.10\,\mathrm{m}$	Vortex radius	$a = 0.0336\,\mathrm{m}$
AF width	$B = 0.20\,\mathrm{m}$		
Mean angle of attack	$\varphi_{\mathrm{m}} = 0$	Dynamic profile quality	$\zeta_{\mathrm{dyn}}(\alpha_{\mathrm{dyn}})$ from [40]
Factor f_{D} for $\theta_{\mathrm{e}} = f_{\mathrm{D}}\theta_{\mathrm{s}}$	$f_{\mathrm{D}} = 1.9796$	(from integration, [3])	

Iteration with varying f (i.e. $2a/R$) in this case is done, till force equality is reached: $\mathrm{H_{mT}}|_{\mathrm{measured}} = \mathrm{H_{mT}}|_{\mathrm{fvm\ calculated}}$. Figure 13 summarizes the input and the resulting plots of three typical quantities over the approximate quarter cycle ($T/4 = 0.049$ s) of the upstroke only, the

- normal velocity $v_{\mathrm{PRN}}(t/T)$, m/s
- horizontal net thrust force $H(t/T)$, N($H =$ Thrust—AF drag > 0 : 'Thrust')
- total power required to pitch the AF in air $P(t/T)$, Watt.

The following four independent quantities are used to define the problem: $\mathrm{Re_{vmax}} = (v_{\mathrm{max}}R/\nu)$, $f = (v_{\mathrm{m}}/v_{\mathrm{max}})$, $\mathrm{Str_m} = (f_{\mathrm{OS}}R/v_{\mathrm{m}})$ and $A_{\mathrm{A}} = \varphi_{\mathrm{o}}$. Looking into detailed vortex dynamics (FVM) in general, we have to determine the following additional, dependent quantities:

Oscillating AF:	The vortex size $(2a/R)$
Fixed AF:	The vortex size $(2a/R)$ and the trailing edge shedding frequency f_{VS}, i.e. $\mathrm{Str} = (f_{\mathrm{VS}}\Delta/v_{\infty})$.

6.4 Advantages and limitations of the FVM

Up to now, quite a number of FVM investigations have been performed covering oscillating AF experiments [5, 23], turbomachine cascade flow, heat transfer and mixing applications [6, 24, 36, 74], free swimming analyses of fish and robots [45] and first approximations for take-off and cruise flight of birds [3, 7].

What experience do we have so far, and what are the advantages and limitations of the FVM?

Advantages

1. The FVM provides consistent physical explanations of vortex formation and resulting force generation. New unsteady flow mechanisms maintain an intermittent smooth flow condition at the trailing edges. The mechanisms are primarily valid for oscillating, and also for fixed AFs. Consistent results are obtained for both, convergent as well as divergent trailing edges.
2. There is a wide range of problems, which can be quickly and efficiently solved: oscillating AFs, supported or freely moving with unsteady flow, characterized by $\mathrm{Re_R} = 10^3 - 10^6$ and $\mathrm{Str_A} = 0.03 - 1.70$. There are preliminary, promising results with consistent data for fixed AFs,

too; without separation and $\mathrm{Re_R} = 10^5 - 10^7$ (realistic trailing edge shedding frequencies f_{VS} given by $\mathrm{Str} = (f_{\mathrm{VS}}\Delta/v_\infty) = 2.2-5.3$). New insights open applications for design by analysis in engineering as well as in nature.

3. The general equations [eqns (7)–(11)] allow the determination of forces, loads, circulation and powers for arbitrary oscillation frequencies, amplitudes and free-stream velocities with reasonable accuracy. Accuracy for force results ranges within $a \pm 20\%$ band, when finite vortex sizes are aproximated by the preliminary relation, given in Fig. 15.
4. The FVM represents a good complement to minimize or avoid large-scale, unsteady NS simulations and/or extensive, costly experiments. So it helps to screen and to prepare efficient, large designs of experiments, both for numerical as well as experimental investigations.
5. Approximate, explicit formulas were derived from conservation of momentum, etc., which is restricted to inertial type forces and powers (Section 6.5). These formulas have been successfully used to simulate the swimming of fish up to now (Section 9).

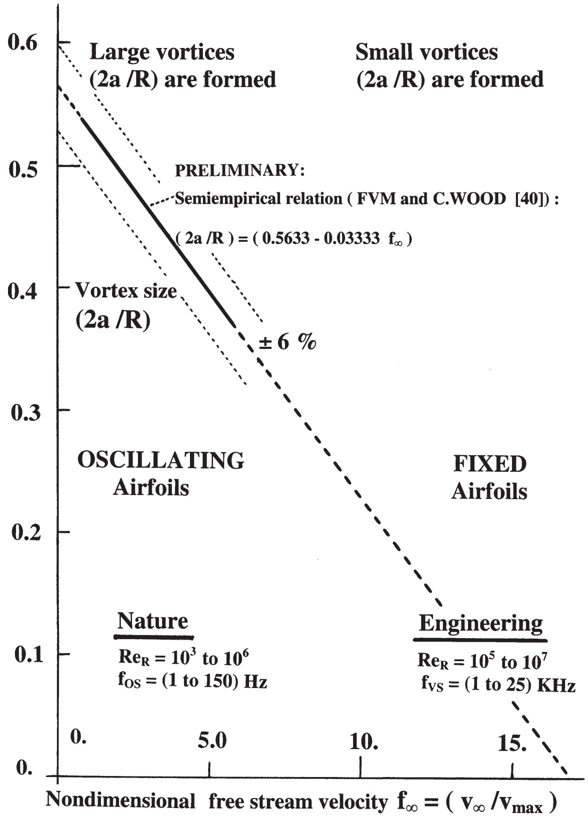

Figure 15: Preliminary semiempirical 'fvm-1' input for approximate vortex size ($2a/R$) as a function of the parameter $f_\infty = (v_\infty/v_{\max})$. The data within $f_\infty = 1$–5. (oscillating AF) was obtained from matching analyzed 'fvm-1' force results with the experimentally obtained forces from Wood [8]. The relation is linearly extrapolated to larger f_∞ up to 15.

Limitations

1. The key parameter $(2a/R)$—the finite vortex size—is a priori unknown. It can be determined experimentally, as has been done here. Possibly there is a characteristic governing relation such as $(2a/R) = f(\mathrm{Re}_{\mathrm{vmax}}, \mathrm{Str}_{\mathrm{m}}, f, A_{\mathrm{A}}, \mathrm{Ma})$, which would be worth identifiying. The semiempirical relation $2a/R(f_\infty)$ in Fig. 15 is preliminary.
2. Wake feedbacks on unsteady forces, etc., are taken care of iteratively and only from the mean, induced jet velocity v_{id}. This jet velocity is approximated by relating the known (finite) mass flow to a meaningfully approximated flow cross section A_{ka} for the v_{id} [see eqns (10)–(11)].
3. The unsteady, complex formation of vortex systems is approximated by one vortex pair only: the dominating TEV plus the compensating BV. Experiments sometimes indicate formations of multiple (though weaker) vortex systems.
4. $F_{2,1}$ and v_{R} are related to the (generally moment free) quarter chord point M. The vortex/AF interaction is strictly 2D. The approximate formulas, in Section 6.5, have so far failed to predict the take-off flight of large birds (Section 9).

6.5 Approximations

Conservation of mass and momentum allow to reduce the general equations [eqns (7)–(11)] and derive an explicit relation, for instance, for the generated mean force H_{mT} [3]. Assuming that two TEV vortex cylinders are detached per cycle, we obtain the partial mass flow (d*m*/d*t*):

$$(\mathrm{d}m/\mathrm{d}t) = 2m_{\mathrm{V}}/T = 2\pi a^2 B\rho f_{\mathrm{OS}}. \tag{12}$$

With a meaningful cross section A_{ka} (see Section 6.2) for this flow, we can approximate the jet velocity $v_{\mathrm{id}} = (v_{\mathrm{out}} - v_{\mathrm{in}})$ and, for harmonic pitching $\varphi(t) = (\varphi_m + \varphi_{\mathrm{o}} \sin \omega t)$ the H_{mT} as follows:

$$A_{\mathrm{ka}} = RB[(2a/R)\cos\varphi_{\mathrm{o}} + 2(R_{\mathrm{eff}}/R)\sin\varphi_{\mathrm{o}}]$$

$$v_{\mathrm{id}} = (\mathrm{d}m/\mathrm{d}t)/\rho A_{\mathrm{ka}} \quad \text{so that} \quad H_{\mathrm{mT}} = (\mathrm{d}m/\mathrm{d}t)^2/\rho A_{\mathrm{ka}} = (\mathrm{d}m/\mathrm{d}t)\,(v_{\mathrm{out}} - v_{\mathrm{in}}) \tag{13}$$

$$H_{\mathrm{mT}} = (\pi^2/4)(2a/R)^4 R^3 B\rho f_{\mathrm{OS}}^2/[(2a/R)\cos\varphi_{\mathrm{o}} + 2(R_{\mathrm{eff}}/R)\sin\varphi_{\mathrm{o}}]. \tag{14}$$

This approximation neglects the rotational momentum plus the circulatory forces $F_{1,2}$. Equation (14) can be rearranged towards eqn (6), giving a thrust coefficient C_{T}:

$$C_{\mathrm{T}} = \mathrm{Str}_{\mathrm{m}}^2\,(2a/R)^4(\pi^2/2)1/[(2a/R)\cos\varphi_{\mathrm{o}} + 2(R_{\mathrm{eff}}/R)\sin\varphi_{\mathrm{o}}] \tag{15}$$

with the dimensionless parameters:

$$\mathrm{Str}_{\mathrm{m}} = (f_{\mathrm{OS}}R/v_{\mathrm{m}}) \quad \text{and} \quad \mathrm{C}_{\mathrm{T}} = \mathrm{H}_{\mathrm{mT}}(2/\rho)(1/v_{\mathrm{m}}^2 RB). \tag{16}$$

It is interesting to look at the plots in Fig. 16, showing full 'fvm-1'calculations and/or oscillating AF experiments in terms of eqn (15). The curves A and C condense all 40 single tests of [2] into single functions: both the vortex sizes $2a/R$ $(\mathrm{Str}_{\mathrm{m}})$ and the corresponding measured thrust coefficients C_{T} $(\mathrm{Str}_{\mathrm{m}})$ show the expected hyperbolic trend. In addition, the mean product $(\mathrm{Str}_{\mathrm{m}}\varphi_{\mathrm{o}}) = 0.7394 \pm 2.5\%$ turns out to be constant for all tests; so does $(\mathrm{Str}_{\mathrm{m}}\ 2a/R)$.

It should be kept in mind that the oscillating AF curves A and C from experiments [2] are covering a wide range of frequencies f_{OS} (≈8–23 Hz) and amplitudes φ_{o} (≈12.5°–30.5°).

Similar curves (Fig. 16, curves B and D) are derived from the FVM application to fixed AFs, as will be shown in the next section.

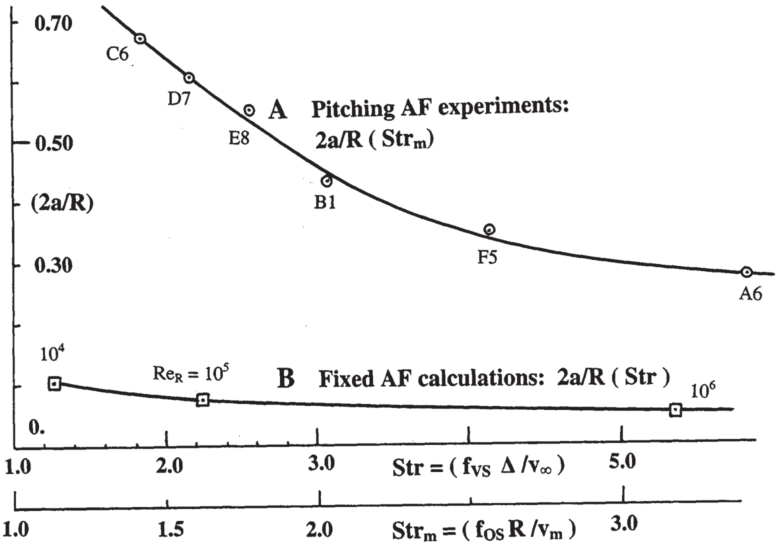

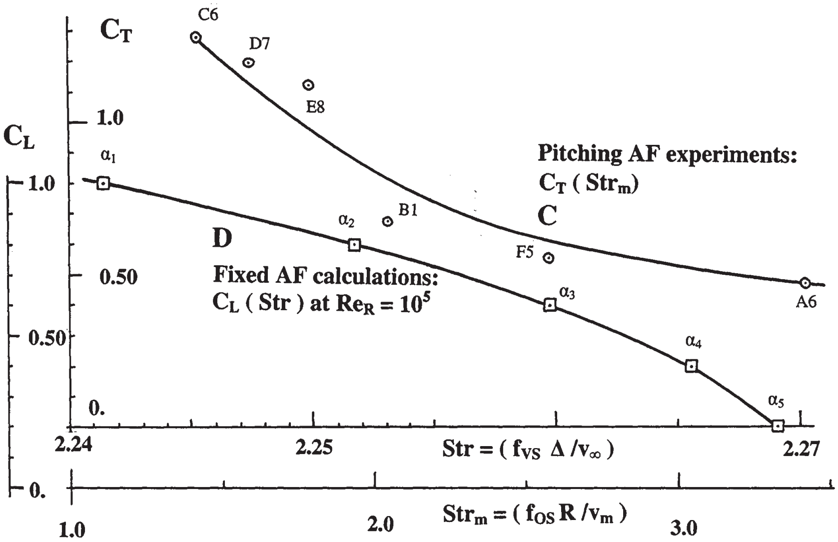

Figure 16: Approximate calculation of the vortex size and force coefficients vs. Strouhal numbers. Top:(A) Vortex sizes $2a/R(\mathrm{Str_m})$ for all 40 pitching AF experiments [2]; (B) Vortex shedding calculations for an airplane wing during take-off with the vortex sizes $2a/R(\mathrm{Str})$. Bottom: (C) Thrust forces $C_\mathrm{T}(\mathrm{Str_m})$ for all 40 pitching AF experiments [2]; (D) lift forces for an airplane wing at $\mathrm{Re_R} = 10^5$ for different angles of attack ($\alpha \approx 2°$–$10°$).

7 The FVM for fixed AFs

Let us consider a classical aircraft wing with a fixed AF in a high free-stream velocity flow v_∞ (see also Fig. 1, curve 1, $\mathrm{Re}_R \approx 10^6$). What is the potential of the FVM, when assuming a high frequency (f_{VS}), free vortex shedding with the intermittent suction mechanism at the trailing edge, as shown in Fig. 11? In contrast to the current practice with a circulation Γ from the Kutta condition, within the FVM we have two unknowns to determine, the f_{VS} and the vortex size ($2a/R$).

Recent NS simulations of Sondak [75] and Zheng *et al.* [47] confirm shedding and predict frequencies f_{VS} of ≈10–25 kHz at the trailing edge of turbomachine cascades. These high f_{VS} are also confirmed by wake fluctuation measurements from Didier [46] and Schobeiri [76] (blade passage frequencies in turbomachines are much lower: ≈1–5 kHz). We also know that there are very thin BL thicknesses in the Re_R range of 10^5–10^7: $(\delta/R) \approx 2\%$–5%, and the trailing edge thickness itself (Δ/R) is around 0.3% [77]. Before applying the FVM, we will take a closer look at the mechanisms in Fig. 11.

7.1 The intermittent suction mechanism

Figure 11 depicts the intermittent suction mechanism in four stages t_1 to t_4, with the following events in detail:

t_1: Starting at a deficit velocity $v_\mathrm{p} > v_\mathrm{s}$ the streamlines are bent by the one-sided suction S, a first TEV_1 is rolled-up at the lower edge; the sharp trailing edge is 'rounded' for the flow.

t_2: Increasing suction/TEV size and rotation accelerate the upper v_s. The RSP moves towards the trailing edge. Due to the fixed AF inclination, the counterrotating vortex from the upper edge is degenerated (it is neglected).

t_3: As part of the self-controlling suction mechanism, a zero deficit is reached now: $v_\mathrm{p} = v_\mathrm{s}$. Thus the smooth flow condition (Kutta) is maintained at the trailing edge. The full TEV size ($2a/R$) and maximum circulation Γ are effective, though unknown. The RSP moves to the trailing edge.

t_4: After detachment of the TEV_1, the RSP jumps back off the trailing edge, and a new TEV_2 rolls up, etc. There is only one counterclockwise TEV shedding per cycle $T = (t_4 - t_1)$. It seems very likely that the maximum TEV size possible is in the order of the trailing edge thickness (Δ/R) plus the two BL thicknesses (δ/R) at the end of the AF, i.e. the vortex size is limited.

This sequence plus analyses suggest that the FVM is able to maintain a high fraction of the theoretical, mathematical Kutta–Joukowski condition at the trailing edge.

7.2 Vortex size and detachment frequency

Due to the limited lee width of $(2\delta + \Delta)$ the maximum vortex size ($2a/R$) must be in that order of magnitude. Assuming that $\max(2a/R) = (2\delta + \Delta)$, and expressing the BL δ by the local, known turbulent or laminar Re_R number [60], we get with $(\Delta/R) = 0.0034$ according to [6, 77],

$$\begin{aligned} &\text{Turbulent:} \quad 2\delta_{\mathrm{turb}}/R = 0.740/\mathrm{Re}_\mathrm{R}^{0.20} \\ &\text{Laminar:} \quad 2\delta_{\mathrm{lam}}/R = 10.0/\mathrm{Re}_\mathrm{R}^{0.50} \end{aligned} \tag{17}$$

$$\max(2a/R) = (2a/R) = (2\delta + \Delta)/\mathrm{R}. \tag{18}$$

With the approximation eqn (14) in the form of eqn (6), the following dimensionless relation is obtained:

$$C_{\mathrm{L}} = \mathrm{Str}_{\infty}\,(2a/R)^2\,\pi\tan\alpha/2. \tag{19}$$

Rewriting eqn (19) with the more appropriate $\mathrm{Str} = (f_{\mathrm{VS}}\,\Delta/v_{\infty})$ for trailing edge vortex shedding and using the above assumptions yields:

$$C_{\mathrm{L}}(\alpha) = \mathrm{Str}(2a/R)^2\,(R/\Delta)\pi\tan\alpha/2. \tag{20}$$

For consistency, we use the (theoretical) relation(s) for C_{L} and the lift force F_{L}:

$$C_{\mathrm{L}}(\alpha) = 2\pi\sin\alpha \quad F_{\mathrm{L}} = C_{\mathrm{L}}(\rho/2)v_{\infty}^2\,RB. \tag{21}$$

7.3 Simulation of airplane flight by the FVM

Take-off and cruise of a small airplane is considered, having the following Input data:

Wing span	$b = 10\,\mathrm{m}$
Mean, constant chord	$R = 1.0\,\mathrm{m}$
NACA profile 0012 with	$\alpha = 10°$ (see Fig. 1)
Corresponding lift coefficient	$C_{\mathrm{L}} = 2\pi\sin\alpha = 1.091$
Total weight of airplane	$F_{\mathrm{W}} = 1500\,\mathrm{N}$
Mean thickness of trailing edge	$(\Delta/R) = 0.0034$
Air properties	$\rho = 1.2\,\mathrm{kg/m^3}$ and $\nu = 15.8 \times 10^{-6}\,\mathrm{m^2/s}$

Two calculations are done in parallel, and the results are summarized in the following table, [eqn (22)]: (1) FVM approach; (2) Conventional approach, employing the Kutta–Joukowski condition.

Parameter	1 Airplane rolling $\mathrm{Re_R} = 10^4$	2 Airplane rolling $\mathrm{Re_R} = 10^5$	3 Airplane take-off $\mathrm{Re_R} = 10^6$
Common results for (1) and (2)	Laminar	Laminar	Turbulent
v_{∞}(m/s)	0.158	1.58	15.8
$\mathrm{F_L}$ (N)	0.1634	16.34	$1634 > 1500 = F_{\mathrm{W}}$
1. FVM approach			
$(2\delta/R)$	0.10	0.0740	0.0467
$(2a/R)$	0.1034	0.0774	0.05009
Str	1.253	2.236	5.338
f_{VS} (KHz)	0.0582	1.039	24.8
2. Conventional approach			
Γ_{Kutta} ($\mathrm{m^2/s}$)	0.08619	0.8619	8.619

(22)

Surprisingly, the simple eqns (17)–(21) of the approximative FVM approach give consistent and plausible results for lift, frequency and vortex size. With the assumed vortex size eqns (17) and (18), we are able to match the known shedding frequencies $f_{\mathrm{VS}} \approx 10$–$25\,\mathrm{kHz}$, obtained both experimentally and numerically. Even the above low $\mathrm{Re_R}$ number result of $f_{\mathrm{VS}} = 58.2\,\mathrm{Hz}$ correlates well with recent measurements of Kesel [78] for $\mathrm{Re_R} = 7000$ and $\alpha = 4°$ reported to be $f_{\mathrm{VS}} = 32\,\mathrm{Hz}$.

The following preliminary lessons from FVM application to fixed AFs within $\mathrm{Re}_{\mathrm{R}} \approx 10^5$–$10^7$ can be summarized (see Figs 15 and 18):

- The intermittent suction mechanism is able to generate sufficient lift for airplanes to take off. Associated typical vortex sizes are $(2a/R) \approx 0.03$–0.10 (see also Fig. 15 and [6]).
- In contrast to human, fixed AF flight, nature utilizes oscillating fins or wings for efficient, simultaneous thrust and lift generation. This concept involves larger vortices, $(2a/R) \approx 0.40$–0.60 (see Fig. 18).
- The proposed 'ladder-wake' for oscillating AFs [3, 7] is also useful to interpret the vortical wake behind aircraft wings: large vortices/small f_{VS} are involved during slow motion of the airplane on the ground. The classical 'starting vortex' is a system of low frequency 'ladder-steps', which gradually get denser (small vortices/large f_{VS}). This wake model can also explain the Wanger effect [79].

Finally, Fig. 16 compares the dimensionless results for the above fixed AF with those obtained for oscillating AF cases earlier: eqn (20) is plotted as curve B, showing $2a/R$ (Str) with a fixed $\alpha = 10°$ (Re_{R} varying with Str). Figure 16, curve D indicates the trend of C_{L} (Str) for a fixed Re_{R} (α varying). Both curves B and D consistently correspond to the earlier ones A and C.

8 Applications of FVM in engineering

The following FVM applications demonstrate the wide range of engineering cases which can be treated (code 'fvm-1'):

- The analysis of pitching and plunging experiments with arbitrary free-stream velocities.
- Quantification of the vortex size from measured forces or vortex circulations.
- FVM applications to come up with alternative profile, trailing edge and wing designs.

8.1 The pitching AF

Figure 17 depicts more details of the pitching AF analyses (Figs 13 and 14) of experiments [2]: the following six quantities are plotted over the dimensionless time $(t/T) = 0.77$–1.02 during the upstroke. The mean value of each quantity over a full cycle $T = 0.049$ s is given in brackets:

Velocities:

- Normal velocity v_{PRN} at the trailing edge (2.1845 m/s)
- Resulting incidence flow velocity v_{R} (0.8308 m/s)

Circulatory forces:

- Transverse (Magnus) force F_2 (0.2024 N)
- AF drag force F_1 (0.1944 N)

Horizontal forces:

- Total force H at the leading edge support (+0.07483 N)
- Inertial force H_{i} at the leading edge support, 60.2% of H (+0.04498 N)
- Circulatory force H_z at the leading edge support 39.8% of H (+0.02975 N)

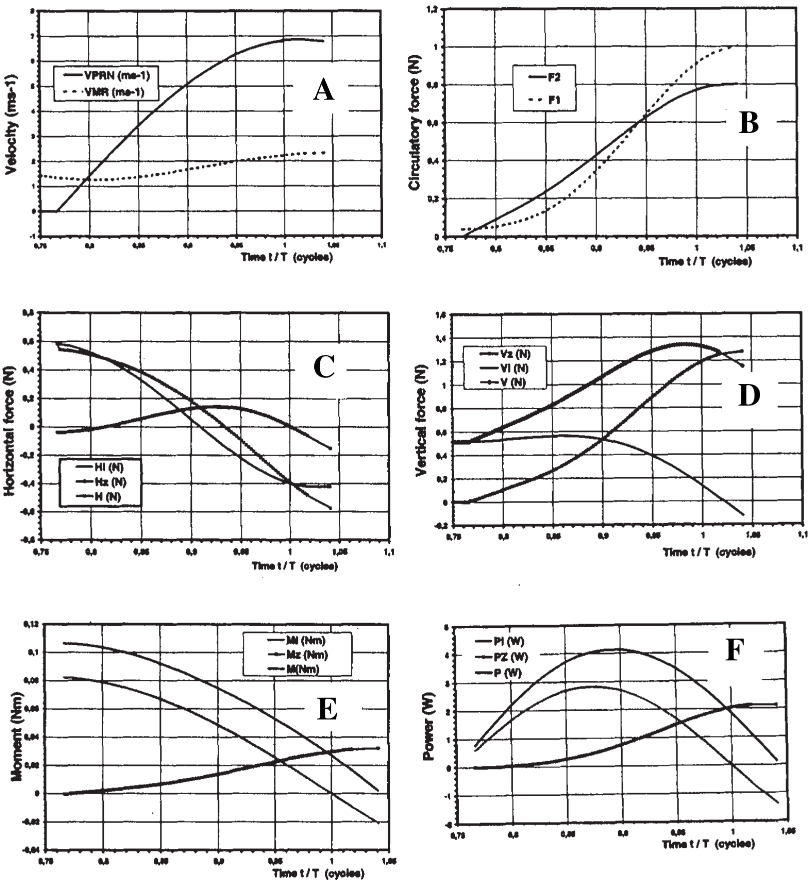

Figure 17: FVM results (2): More data on the performance of the pitching AF of Fig. 13 over the approximate quarter cycle (analysis of the case C6 of the experiments [2]) with time-dependent quantities. (A) Velocities: Normal velocity v_{PRN} at trailing edge; resultant incidence velocity $v_{\mathrm{MR}} = v_{\mathrm{R}}$ at the quarter chord point. (B) Circulatory forces: Magnus force F_2, AF drag force F_1 from ζ_{dyn}. (C and D) Horizontal and vertical forces at the left AF end '1': overall H, V; inertial H_{i}, V_{i} and circulatory component H_z, V_z. (E) Moments: External driving moment M; internal inertial/circulatory component of moment M_i/M_z (F) Powers: Externally required total driving power P; internal inertial/circulatory power components P_i/P_z.

Vertical forces:

- Total force $\pm V$ at the leading edge support ($\pm 1.001 \equiv 0$ N)
- Inertial force $\pm V_{\mathrm{i}}$ at the leading edge support, 44.3% of V ($\pm 0.4433 \equiv 0$ N)
- Circulatory force $\pm V_z$ at the leading edge support, 55.7% of V ($\pm 0.5572 \equiv 0$ N)

Main moments:

- External driving moment M (± 0.07270 Nm)
- Inertial moment M_{i}, 64.2% of M (± 0.04668 Nm)

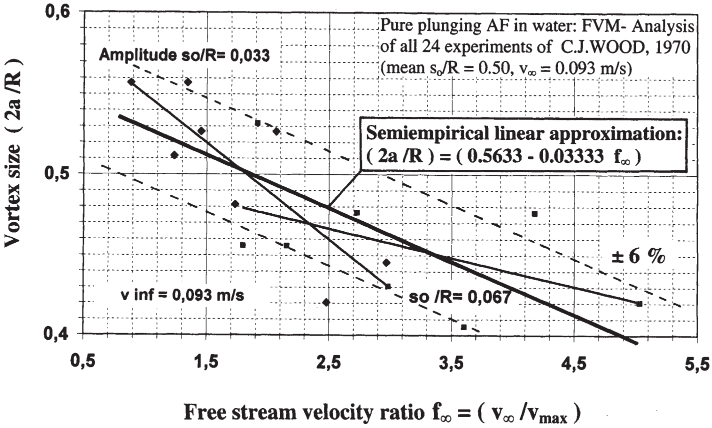

Figure 18: Finite vortex size ($2a/R$) from FVM analyses of plunging AF experiments [8].

- Circulatory moment M_z, 19.2% of M (± 0.01393 Nm)
- Rotational moment M_B, 16.6% of M

Main powers:

- Total driving power required P (1.508 W)
- Inertial power P_i, 58.1% of P (0.8758 W)
- Circulatory power P_z, 28.0% of P (0.4226 W)
- Rotational power P_B, 13.9% of P

8.2 The plunging AF with arbitrary free-stream velocities

Purely plunging experiments with an NACA 0012 in water were published by Lai and Platzer [35]. Vortex visualizations with color injection revealed varying wake patterns: Drag-type, neutral and thrust-type von Karman streets, but no forces, were measured. Figure 19 depicts four cases A–D, with A and B taken from the experiments [35]. Wake patterns of A and B are of the 'neutral' and 'thrust' type, respectively, as shown in Fig. 19. The FVM results are also shown in a table. Main findings below indicate that it takes higher frequencies f_OS and amplitudes s_o (i.e. lower $f = (1/\mathrm{Str}_{\mathrm{A,m}}))$ to generate the net thrust forces ($H_\mathrm{mT} > 0$), than realized in the plunging tests. Thus a 'thrust'-type wake pattern must not necessarily mean $H_\mathrm{mT} > 0$ (case B):

	$\mathrm{H_{mT}} < 0$: Drag		$\mathrm{H_{mT}} > 0$: Thrust	
Case	A	B	C	D
Input:				
R (m)	0.10	0.10	0.010	0.10
v_∞ (m/s)	0.20	0.20	0	0.60
			but $v_\mathrm{in} = 0.0656$ m/s	
			($f_\mathrm{in} = 0.4227$)	

f_{OS}	2.50	5.00	10.0	20
s_{o} (mm)	5.00	10.00	2.47	36.4
Output:				
$f = (v_{\mathrm{m}}/v_{\max})$	10.72	3.544	0.4882	0.3329
H_{mT} (N)	−3.499	−9.409	+0.00163	+30.24
P_{mT} (W)	0.02668	0.8787	0.003554	679.4
(2a/R) from eqn (23)	0.4549	0.5421	0.5492	0.5590

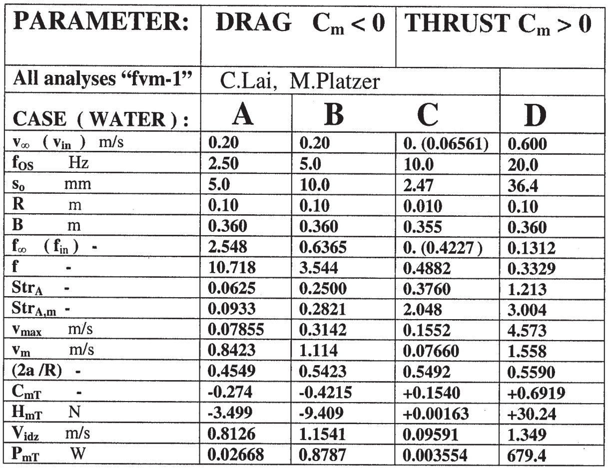

PARAMETER:	**DRAG $C_m < 0$**		**THRUST $C_m > 0$**	
All analyses "fvm-1"	C.Lai, M.Platzer			
CASE (WATER) :	**A**	**B**	**C**	**D**
v_∞ (v_{in}) m/s	0.20	0.20	0. (0.06561)	0.600
f_{OS} Hz	2.50	5.0	10.0	20.0
s_o mm	5.0	10.0	2.47	36.4
R m	0.10	0.10	0.010	0.10
B m	0.360	0.360	0.355	0.360
f_∞ (f_{in}) -	2.548	0.6365	0. (0.4227)	0.1312
f -	10.718	3.544	0.4882	0.3329
Str_A -	0.0625	0.2500	0.3760	1.213
$Str_{A,m}$ -	0.0933	0.2821	2.048	3.004
v_{max} m/s	0.07855	0.3142	0.1552	4.573
v_m m/s	0.8423	1.114	0.07660	1.558
(2a /R) -	0.4549	0.5423	0.5492	0.5590
C_{mT} -	-0.274	-0.4215	+0.1540	+0.6919
H_{mT} N	-3.499	-9.409	+0.00163	+30.24
V_{idz} m/s	0.8126	1.1541	0.09591	1.349
P_{mT} W	0.02668	0.8787	0.003554	679.4

A **Amplitude $s_o = 5.0\mathrm{mm}$, $f_{OS} = 2.50$ Hz, $v_\infty = 0.20$ m/s, f = 10.72, (2a /R)= 0.2274, $H_{mT} = -3.499$ N, $P_{mT} = 0.02668$ W, $Str_{A,m} = 0.0933$**

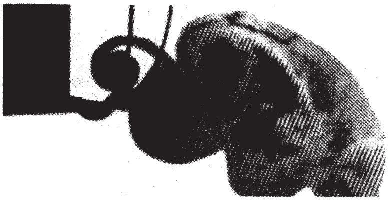

B **Amplitude $s_o = 10.0\mathrm{mm}$, $f_{OS} = 5.0$ Hz, $v_\infty = 0.20$m/s, f = 3.544, (2a /R)= 0.2710, $H_{mT} = -9.409$ N, $P_{mT} = 0.8787$ W, $Str_{A,m} = 0.2821$**

Figure 19: Purely plunging AF experiments of J. Lai *et al.* [35]: Cases A and B with drag-type wake patterns. FVM analyses of cases A-D, with mean thrust/drag ($H_{\mathrm{mT}} >$ or < 0) mean required power P_{mT}, induced jet velocity v_{idz}, etc., over a wide range of operation.

8.3 Vortex size from experiments with measured circulation

Wood *et al.* [8] systematically studied plunging AF wakes, and they developed a special method to measure the circulation of visualized, individual vortices in the wake. These data allow the determination of the reaction force exerted on the AF. All tests are FVM analyzed, and $(2a/R)$ iterations are done, until force-equality is reached: $H_{\mathrm{mT}}|_{\mathrm{test}} = H_{\mathrm{mT}}|_{\mathrm{fvm\ analysis}}$. Figure 18 shows the findings $2a/R$ (f_∞) for two amplitudes s_o, [5]. The resulting regression function for the mean amplitude $(s_\mathrm{o}/R) = 0.5$ turns out to be:

$$(2a/R) = (0.5633 - 0.03333 f_\infty) \pm 6\,\%. \tag{23}$$

Up to date, this semiempirical relation represents a simple, though preliminary approximation of the vortex size under similar conditions. Additional influences from $\mathrm{Re}_{\mathrm{vmax}}$, $\mathrm{Str}_\mathrm{m}, f, A_\mathrm{A}$ and Ma are expected. Future investigations should address this topic.

8.4 FVM applications for improved fixed AF designs

Up to now, the discussion of the FVM vortex dynamics in globally steady and unsteady aerodynamics revealed some new insights towards physical understanding and design improvements for fixed AFs. Two fields of application are given, concerning improved profile and wing designs: the concept of 'backflow barriers' on profiles (Fig. 20) and contributions to the idea of a so-called 'diverging trailing edge' (DTE, Figs 21 and 22).

8.4.1 The 'backflow barrier'

High performance glider airplanes use flexible, self-actuating flaps on the suction side, which act as 'backflow barriers', observed in nature and described by W. Liebe, [22]. First successful tests were performed on a Me 109 in 1939, and broad investigations followed 40 years later by Bechert [25] and Rechenberg [28]. Figure 20 depicts such a self-controlling flap BB with the associated lift enhancement from C_L (α), and the observed flow pattern. The movable BB pops up in low velocity flight situations with high α (take-off, landing), preventing a backflow of air at the stall point. The resulting performance improvements are remarkable ($\mathrm{Re}_\mathrm{R} \approx 10^5$–$10^6$) : $\approx$ 10%–30% increase of lift, a delayed stall (α_{SS} from 20° to 35°) and a more forgiving characteristic $C_\mathrm{L}(\alpha)$. The globally steady BB flow seems to involve two mechanisms (authors opinion):

- The profile is 'rounded' and it is easier for the flow to 'bend' at high α without separation. A concentrated, well trapped and steady LEV is driven by v_∞ separated from a second bound, central vortex (CV) between the BB and the RSP. In the compensating vortex pair TEV/BV (Thomson), the BV represents the sum (LEV + CV).
- Both LEV and CV are positioned between the FSP and the RSP; they are the lift generating BVs, and they are both effectively protected against fluid in-rush into their low pressure core. Lift generation does not break down.

It is interesting to examine the early AF/flap/slat combinations proposed by Kasper [37], where similar mechanisms seem to be involved.

8.4.2 The diverging trailing edge

The trailing edge geometry is crucial for maximum lift and forgiving stall behavior. Conformal mapping tells us to keep the trailing edge as thin as possible. Unsteady aerodynamics and vortex

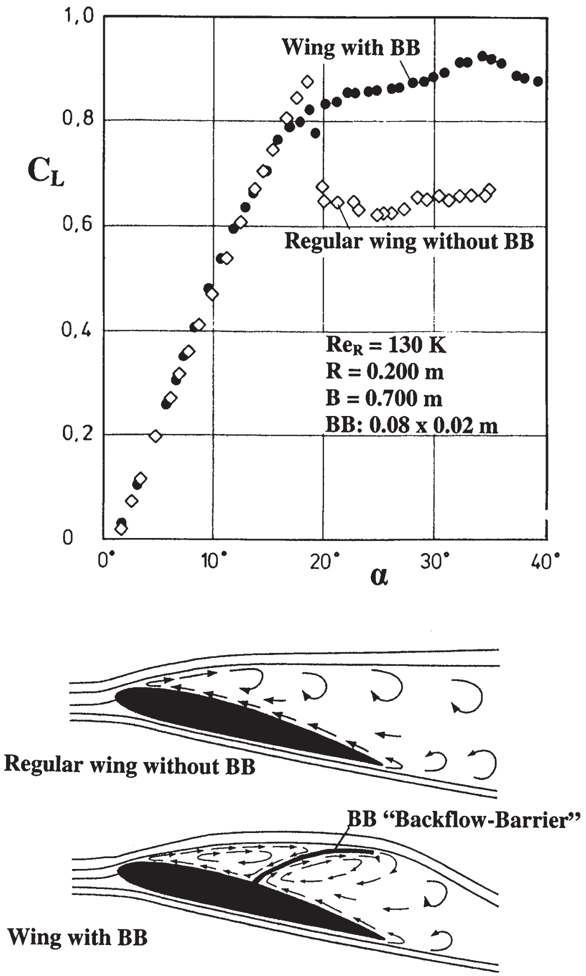

Figure 20: Engineering application (1): The self-actuating flap or 'backflow barrier' protects and stabilizes the lift enhancing LEV. First idea and successful testing on a Me 109 in 1939 W. Liebe [22]. The data $C_L(\alpha)$ shown are taken from experiments [28, 72]. See also recent studies [25, 27].

interaction, however, 'modify' this opinion, and they are able to explain the better performance of a DTE. Figure 21A–D compares current trailing edge designs for aircraft and turbomachine applications:

(A) Commercial aircraft Airbus A340-300, having a conventional, converging, thin trailing edge with $(\Delta/R) = 0.0034$ [77]. High performance fighter jets have a thicker $(\Delta/R) = 0.010$.

(B) Heavy duty gas turbine, having inner-cooled turbine blades and vanes. Efficient inner air cooling requires thick trailing edges with $(\Delta/R) = 0.0270$ [36].

(C) Conventional aircraft trailing edge design with an improving Gurney miniflap, representing a DTE. Its height is within approximately half the BL displacement thickness ($\mathrm{Re}_R = 10^6$): $(h/R) = 0.017$ and $(d/R) = 0.0025$ [26].

(D) Details of the flow pattern behind a DTE [36], showing flow acceleration due to a large ($p_\mathrm{P} - p_\mathrm{S}$), a strong TEV with a 'saddle point' SP, a shifted RSP and an additional upper vortex UV.

The Gurney invention originates from the design of racing cars [80]. Later on Bechert *et al.* [26] and Kesel [78] found similar 'microflaps' (with 'spades' as vortex generators) on dragonfly wings. Lift enhancements of ≈ 20–25% are common on DTE and Gurney flap wings at $\mathrm{Re}_\mathrm{R} \approx 10^6$, while C_D increases only slightly.

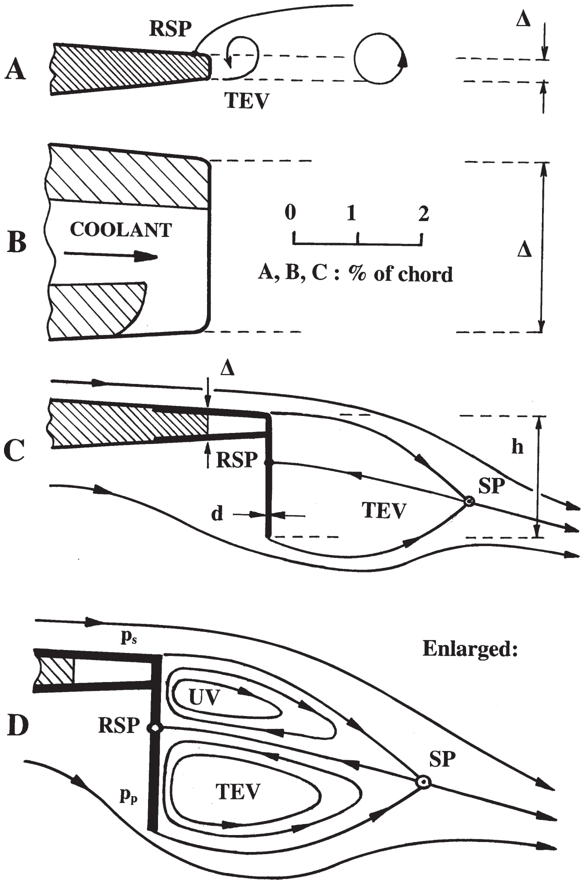

Figure 21: Engineering application (2): Current and improved trailing edge designs with DTE [26, 78]. (A) Current commercial aircraft: A340-300 trailing edge with $(\Delta/R) = 0.0034$ [77]; fighter jets have a $(\Delta/R) = 0.010$. (B) Current heavy duty large gas turbines: inner cooling of the vanes/blades requires intensive edge cooling, i.e. thick trailing edges with $(\Delta/R) = 0.027$. (C) Improved trailing edge design, using a Gurney miniflap (a DTE design [26]) with $(h/R) = 0.017$ and $(d/R) = 0.0025$. (D) Enlarged view of the flow details behind the DTE in (C), with a high accelerating ($p_\mathrm{P} - p_\mathrm{S}$), a strong TEV, a 'saddle point' SP, a shifted RSP and a small upper vortex UV [36].

Since about 1995, DTEs have been successfully used in aircraft and wind turbine engineering. The enlarged complex flow pattern in Fig. 21D [36] is characterized by a higher static pressure p_{P}, raising $(p_{\mathrm{P}} - p_{\mathrm{S}})$. This accelerates and deflects the lower flow and rolls up a strong TEV due to a high v_{N}. The blunt trailing edge builds up a SP within the fluid downstream, and the RSP moves around the corner. Therefore, an additional bound UV is formed, which is part of the overall BV system. The vortices are well trapped by the SP, but some instability causes a sideways swinging of the whole system, while the TEVs are shed with f_{VS}. The stronger the TEV/suction and the lower the average position of the SP, the higher is the beneficial deflection $\Delta\alpha$ of the upper flow ($\alpha_{\mathrm{DTE}} = \alpha + \Delta\alpha$). In addition, due to the SP position downstream, the effective AF chord is enlarged to $R_{\mathrm{DTE}} = R + \Delta R$: the overall effect is a large increase of C_{L} and a delay of stall. One important DTE design objective is to suppress those instabilities (swinging) by damping devices and interruptions, adding three-dimensionality [26].

8.4.3 Some newly proposed DTE designs

Figure 22 indicates selected DTE variants [36] which are partly inspired by the dragonfly wing structure and partly by the expected unsteady vortex dynamics (Figs 9–11).

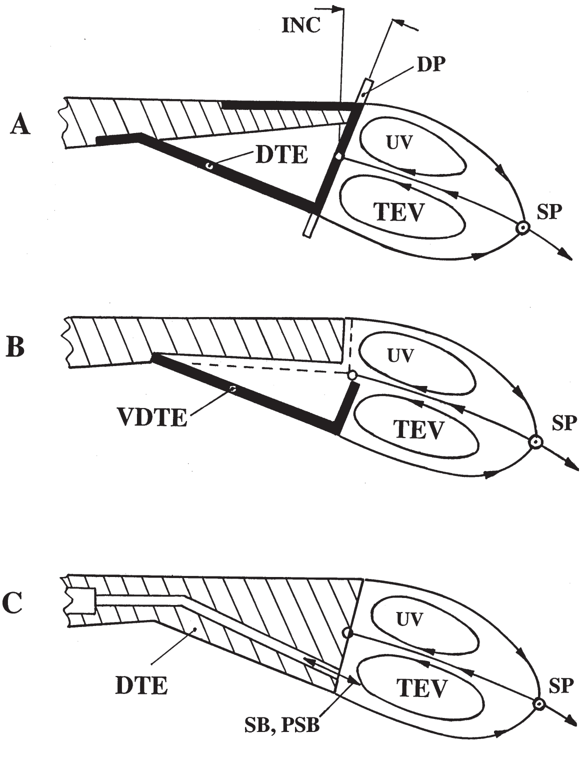

Figure 22: Engineering applications (3): Newly proposed DTE designs for high lift, delayed stall and low noise [36]. (A) Inclined DTE (INC) with damping protrusions (DP) and stabilizing spanwise interruptions (I). (B) Variable divergence trailing edge (VDTE) for high and low velocity flight (short interruptions, small inclination only). (C) Inclined DTE with an enhanced TEV by superimposed blowing (SB) and/or periodic suction and blowing (PSB).

Different combinations from [36] show the following features in Fig. 22A–C [26, 30, 33, 47, 78]:

- damping protrusions (DP) to suppress the instabilities (smaller $d(\Delta\alpha)/\mathrm{d}t$);
- interruptions (I) and slits to stabilize the sideways swinging (added three-dimensionality);
- variable divergence trailing edge (VDTE) for cruise as well as slow flight during vertical take-off and landing (VTOL);
- strengthening of the TEV/suction by inclination (INC) and by using static blowing (SB) and/or periodic suction and blowing (PSB).

9 Applications of FVM in nature

There is a large diversity of solutions for swimming and flying of animals in water and air [65, 81]. The size of living water animals covers a range of 1 : 30000 (larva of zebra fish [82] to blue whales [83]) with the following parameters:

Animal, swimming in water	$\mathrm{Re}_{\mathrm{vmax}}$	$\mathrm{Str}_{\mathrm{A}}$	f_∞
Larva of zebra fish	0.832×10^3	0.139	0.950
Blue whale	3038×10^3	0.513	0.282

Flyers in air need to be much lighter (smaller), and their sizes, cover a range of 1:2000 only (fruit fly [84] to the wandering albatross [85]) with the corresponding parameters:

Animal, flying in air	$\mathrm{Re}_{\mathrm{vmax}}$	$\mathrm{Str}_{\mathrm{A}}$	f_∞
Fruit fly	3.56×10^3	0.0445	0.660
Wandering albatross	69.1×10^3	0.0208	3.650

Compared to locomotion in water, the flyers in air need higher frequencies f_{OS} and amplitudes, for two reasons: first, they have to carry their weight and generate thrust simultaneously; secondly, they have to generate lift and thrust in a low density fluid (air : water $\approx$ 1 : 1000). For efficiency, most flyers and swimmers operate in a rather narrow (frequency × amplitude) range of $\mathrm{Str}_{\mathrm{A}} \approx 0.10$–$0.20$ [86]. Flying was 'invented' twice: very early by the insects, much later by birds, etc., arriving at largely the same solutions ('convergent evolution').

9.1 Swimming in water

Swimming in nature is either using the drag-based principle [moving appendages, paddles or scoops (turtles, manatees, etc.)] or—later in evolution—the lift-based, more advanced hydrodynamic principle (fish, dolphins, whales). The most effective lift-based swimming in water employs the caudal fin propulsion in fish [2, 3, 38, 81, 87], which relies on the efficient generation and management of large vortices and their subsequent wake. Hydrodynamic lift/thrust forces are produced by high performance oscillating (pitching, plunging) fins with the following features:

1. high normal flow velocities $v_{\max}$ around the moving, sharp-edged trailing edge of the fin;
2. optimum selection of pitching, plunging and phase angle between both;

Figure 23: A large killer whale (*Orcinus orca)* from [88]: Strong horizontal fluke for caudal fin propulsion. This whale is 4.7 m long, and it reaches cruise velocities of $v_S \approx 6$ m/s.

3. long trailing edge extension B; thin, elastic (fringes) parts at the end of the fin; slender, elastic body;
4. optimum combination of: f_{OS}, s_o, φ_o, φ_m, R, R_{eff} and ψ; nonharmonic kinematics;
5. concentration of strong (red) musculature in the medial and anterior portions of the body.

Figure 23 shows a large killer whale (*Orcinus orca*) from [88], with its long trailing edge extension, horizontal fluke. The morphology and kinematics of whales and dolphins are well documented and correlated to swimming performance by Fish [83]. Corresponding regression functions for medium to large whales are used next, to analyze the swimming performance of a whale.

9.2 Swimming analysis of a large whale

The approximation eqn (14) for the thrust force H_{mT} is now 'tested' for a representative swimming performance analysis. The following general iterative steps are taken:

1. Set the individual's body length L (within one family) and a desired swimming velocity v_S for the regression parameter (v_S/L); determine individual body geometry from general proportions for that family. Choose ρ and ν for the fluid.
2. Plug (v_S/L) into the regression functions for frequency f_{OS}, pitching amplitude φ_o, trailing edge excursion amplitude h_o for that family.
3. Compute the thrust, power, etc., from the FVM [here for simplicity the thrust eqn (14) only]; determine all quantities needed:

$$\begin{array}{llll} R_{eff} = h_o/\sin\varphi_o & \mathrm{Re}_L = (Lv_S/\nu) & C_D(\mathrm{Re}_L) & \text{from [83] etc.} \\ v_{max} = R_{eff}\varphi_o 2\pi f_{OS} & f_\infty = (v_S/v_{max}) & 2a/R(f_\infty) & \text{from eqn (23).} \end{array} \qquad (24)$$

4. Balance thrust and drag at v_S: $H_{mT} = F_D = C_D\,(\rho/2)v_S^2\,(\pi D^2/4)$ to give v_S (with D as the maximum effective body cross-section diameter).
5. Compare the v_S from step 4 with the initial one from step 1. Iterate till convergence.

The following data are obtained for the largest living animal, the blue whale (after four iterations)

1. $L = 30\,\text{m}$ $v_S = 1.0\,\text{m/s}$ $(v_S/L) = 0.03333$ $\rho = 1000\,\text{kg/m}^3$
   $(B/L) = 0.13$ $B = 3.9\,\text{m}$ $\nu = 1.012 \times 10^{-6}\,\text{m}^2/\text{s}$
   $(R/L) = 0.0289$ $R = 0.867\,\text{m}$ $(D/L) = 0.207$ $D = 6.21\,\text{m}$

2. $f_{OS} = 0.892 + 0.613\ (v_S/L)\,\text{Hz}$ $f_{OS} = 0.9124\,\text{Hz}$
   $\varphi_o = 43.373 - 11.448\ (v_S/L)$ degree $\varphi_o = 43.0$ degree
   $h_o = 0.564 - 0.056\ (v_S/L)\,\text{m}$ $h_o = 0.5621\,\text{m}$ $R_{eff} = 0.824\,\text{m}$

3. $Re_L = 2.96 \times 10^7$ $C_D = 0.020$; $Re_{vmax} = 3.038 \times 10^6$; $Str_\infty = 0.791$ $Str_A = 0.513$
   $v_{max} = 3.55\,\text{m/s}$ $f_\infty = 0.2820$ $(2a/R) = 0.5539$

4. $H_{mT} = 288.8\,\text{N}$ yielding $v_S = 0.976\,\text{m/s} \approx 1.0\,\text{m/s}$ (loop closed)

These consistent and plausible results correspond to earlier FVM analyses for swimming of fish. They indicate that even the simple, inertial approximation eqn (14) appropriately describes caudal fin propulsion in fish.

9.3 Flying in air

It is much more challenging to fly in a low density fluid because not only thrust F_T but at the same time lift F_L has to be generated. On top of this, nature has solved the problem of VTOC from the ground as well as from water surfaces (VTOL with $v_\infty = 0$). The focus of evolution has been on additional measures (compared to swimmers) such as balancing lift and weight, as well as thrust and drag:

- use alternative and more complex kinematics;
- utilize and refine the light weight design principles;
- develop additional mechanisms to manage the challenging low velocity situations (VTOL).

A very strange bird is the sea parrot [89], which can fly in two extremely different fluids, in air as well as in water. When flying in air, the water-wing frequency is raised by a factor of ≈18 (to ≈11 Hz) and the water amplitude is roughly tripled. The buoyancy lift in water has to be counteracted by a 'negative hydrodynamic lift' from the wings. Though the wing design must be an aero- and hydrodynamic compromise, the sea parrot is a perfect example of nature's utilization of 'multi-target' design principles: the bird has, for instance, the competitive advantage of almost unlimited supply of prey from land, sea and air.

9.4 Solutions for flying in air

A closer look at the specific principles of flyers compared to swimmers reveals the following details of force generation towards solutions for cruise flight and VTOL:

- High normal flow velocity v_N and trailing edge extension B: Going from the fin to the wing principle (flapping axis = body axis). Comparing typical wing/fingeometries (f_{OS}, amplitude and chord kept constant) yields a factor of 10–50 higher v_{max}, and v_{R}, levels. In addition to the wing principle, both frequency f_{OS} and flapping amplitude β_{o} are raised in air.

- Complex wing kinematics: A sophisticated 3D superposition of the following kinematic modes is achieved
  - — pitching $\varphi(t)$ of the chord, mostly around the leading edge;
  - — wing flapping 'vertical' $s_{\mathrm{V}}(t) =$ plunging of leading edge; varying in spanwise direction via $\beta(t)$;
  - — wing flapping 'horizontal' $s_{\mathrm{H}}(t) =$ sculling of …via $\beta(t)$;
  - — 'propeller rotation' of the whole bird (wings kept as a 'propeller'); bursts of rotation around the body axis (author's observation on swallows).

    In addition, higher lift F_{L} from system optimization such as
  - — slower downstroke (active, force producing stroke with maximum residence time Δt_{a}) and faster upstroke;
  - — optimum combination of f_{OS}, β_{o}, φ_{o}, φ_{m}, ψ, b and R;
  - — nonharmonic kinematics $\varphi(t)$, $\beta(t)$, etc.;
  - — elastic wings and trailing edge portions.
- Light weight, high energy efficiency: Hollow bones, thin-walled external skeleton. Endothermic design and thermal insulation for muscle efficiency. Internal bone cooling. Wing motion in 'aeroelastic resonance' to save power.
- Simultaneous generation of a high F_{L} and F_{T}: Special techniques for a fast roll-up of a strong TEV with a high Γ (Magnus force F_2) and a high v_{m} (in spite of $v_\infty = 0$ during VTOL). Higher f_{OS}, β_{o} and φ_{m} levels for VTOL; very high φ_{m} shortly before landing. Steady fixed wing lift saves power during cruise flight.
- Devices for high lift/thrust, low drag and low noise: Profile camber, rounded trailing edge, thin and/or diverging trailing edge Wing–tail interaction. Hairs to generate turbulence (delay separation). Birds: Light, stiff feathers, slats, forked wing tips, backflow barriers, spanwise fences, etc. Insects: Structured chitin surface (turbulence, low drag), tripping edges, vortex generators.
- Variable wing/tail geometry: Feathers increasingly specialized, from thermal insulation to aerodynamics with permeable wings employing a 'louver-type' feather action (closing for high-lift downstroke, opening for upstroke). Variable wing span (large b for downstroke). Tandem pair of wings in opposite or parallel motion (insects). Special 3D shoulder joints for 180° turns of wings for efficient hovering (hummingbirds).
- Interaction of flows: Utilization of formation flight, ground effect and the combination of gliding and active flapping flight.

9.5 Analysis of the take-off/cruise flight of a large heron

There is little complete published data on bird flight calculations (forces, power requirements, etc.), partly due to the complex unsteady aerodynamics and partly due to a lack of understanding and/or availability of physical models.

Figure 24 shows a large *Goliath Heron* during take-off (bottom) and landing (top)—the most challenging flight situations. The photos are taken from Rüppell [90], and several high-lift devices can be clearly seen in action:

- forked wing tips are 'fully open' [72];
- leading edge slats at mid-wing position are 'opened' [15];

- multistage backflow barriers are fully popped up [22];
- parallel fences activated to reduce spanwise outward flow.

The FVM so far has been applied to birds' flight in an approximate manner only [3, 7]—the code 'fvm-1' is primarily designed for 2D pitching and plunging AF oscillations. Similarly, we base our flight analyses here on the approximative eqn (14) with the following additional assumptions:

- The trailing edge of the wing is moving in a straight line with an equivalent, purely plunging mode; its amplitude (reference position: 75% of half wing span, i.e. $y = \pm(3/8)\ b$) then is $h = \pm(3/8)b \sin \beta_0$.
- Constant wing span b and chord R. Superposition of pitching and plunging for $v(y, t)$.

Figure 24: A large *Goliath Heron*, photos from Rüppell [90] Bottom: Bird taking off; Top: Landing or slow flight, showing the light feathers on the suction side (SS) activated as 'backflow barriers' [22], slats on the leading edge and fences on the SS [72], forked wing tips [15] and the interaction between wings and tail [65].

- The maximum trailing edge normal velocity $v_{\max}$ is calculated separately from $dv(y,t)/dt \equiv 0$ in $v(y,t) = 2\pi f_{\mathrm{OS}} R\,[(-y/R)\beta_{\mathrm{o}} \sin \omega t + \varphi_{\mathrm{o}} \cos \omega t]$, yielding the corresponding time (ωt^{*}) to reach $v_{\max}$ from
$$(\omega t^{*}) = \arctan[-3/8(b/R)(\beta_{\mathrm{o}}/\varphi_{\mathrm{o}})]. \tag{25}$$
$$v_{\max} = v(\pm 3/8b, t^{*}) = 2\pi f_{\mathrm{OS}} R[-3/8\,(b/R)\beta_{\mathrm{o}} \sin \omega t^{*} + \varphi_{\mathrm{o}} \cos \omega t^{*}]. \tag{26}$$
Here the optimum is assumed to be fixed: pitching advances plunging by $\psi = 90°$.
- The corresponding effective frequency $f_{\mathrm{eff}} = v_{\max}/(2\pi h)$ is inserted into the analogue of eqn (14), yielding:
$$H_{\mathrm{mT}} = (\pi^{2}/4)\,(2a/R)^{3}\, R^{3}\, b\, \rho f_{\mathrm{eff}}^{2} \text{ (here we have used for the whole 'free' wing: } A_{\mathrm{F}} = A_{\mathrm{ka}} = 2ab) \tag{27}$$

The three unknowns t^{*}, $v_{\max}$ and H_{mT} can be calculated from eqns (25)–(27).

The following input from Herzog [85], is used for the large heron:

General input	Take-off input	Cruise input
$b = 1.90\,\mathrm{m}$	$f_{\mathrm{OS}} = 5.0\,\mathrm{Hz}$	$f_{\mathrm{OS}} = 2.75\,\mathrm{Hz}$
$R = 0.25\,\mathrm{m}$	$\beta_{\mathrm{o}} = 70°$	$\beta_{\mathrm{o}} = 50°$
$2a/R$ from eqn (23)	$\varphi_{\mathrm{o}} = 20°$	$\varphi_{\mathrm{o}} = 20°$
$\rho = 1.20\,\mathrm{kg/m^{3}}$	$\gamma_{\mathrm{CL}} = 75°$	$C_{\mathrm{D}} = 0.075$
$m_{\mathrm{B}} = 3.0\,\mathrm{kg}$, so that		$C_{\mathrm{L}} = 0.90$
$F_{\mathrm{W}} = 29.4\,\mathrm{N}$		
$D = 0.753\,\mathrm{m}$		

The following results are obtained iteratively:

Take-off results	Cruise results
$(\omega t^{*}) = 84.3°$	$(\omega t^{*}) = 84.3°$
$v_{\max} = 107.8\,\mathrm{m/s}$	$v_{\max} = 41.7\,\mathrm{m/s}$
$f_{\infty} \approx 0$: $(2a/R) = 0.5633$	$F_{\mathrm{L}} = F_{\mathrm{W}}$ requires: $v_{\mathrm{F}} = 10.7\,\mathrm{m/s}$
$f_{\mathrm{eff}} = 25.62\,\mathrm{Hz}$	$f_{\infty} = 0.2567$: $(2a/R) = 0.5474$
$H_{\mathrm{mT}} = 10.31\,\mathrm{N}$	$f_{\mathrm{eff}} = 12.16\,\mathrm{Hz}$
$F_{\mathrm{L}} = H_{\mathrm{mT}} \sin \gamma_{\mathrm{CL}} = 9.96\,\mathrm{N}$	$H_{\mathrm{mT}} = 2.22\,\mathrm{N}$
$< F_{\mathrm{W}} = 29.4\,\mathrm{N}$	$F_{\mathrm{T}} = H_{\mathrm{mT}} = F_{\mathrm{D}}$ requires: $v_{\mathrm{F}} = 10.5\,\mathrm{m/s}$ (loop closed)

The cruise flight results are consistent and meaningful. The inertial approximation eqn (27) from a simple momentum balance seems to describe that flight condition properly. The take-off flight condition, however, results in a lift force F_{L}, which represents only 34% of the required level to carry the full weight F_{W}. Apparently, eqn (27)—neglecting circulatory forces $F_{1,2}$—is not sufficient to properly model the take-off of the heron. In fact, a rough estimate of the expected Magnus force F_{2} yields a peak $F_{2} \approx 85\,\mathrm{N}$.

We conclude that the FVM approximation eqn (27) is not appropriate to model the heron's take-off. It is very likely that the challenging zero free-stream flight condition additionally takes advantage of the circulatory contributions $F_{2,1}$. Fast spinning of the TEV (high Γ) generates a large $v_{\max}$ and v_{m} (in spite of $v_{\infty} \equiv 0$), and—in conjunction with the wing principle—a large v_{R} is generated. Altogether this results in significant force levels $F_{2,1}$.

10 Conclusions

The paper describes the unsteady flow mechanisms in fluid dynamics, since—strictly speaking—there is hardly a steady flow in real fluids. High/low Re number flow around oscillating and fixed bodies is surveyed to focus the discussion on flow separation, periodic vortex roll-up/shedding as well as the generation of time-dependent forces. In this context, it appears that currently the role of the BL is overestimated in explaining separation and vortex formation.

Starting with the 'edge flow mechanism', a general condition is formulated, which—via viscous, inertial and pressure forces—governs the flow across sharp edges or along curved surfaces. To obtain more insight into the unsteady generation of lift and thrust, this condition is used to replace the current mathematical Kutta relation for the trailing edge of an AF.

This leads to the 'finite vortex model', its justification for the dynamic modeling of the fluid–structure interaction and a detailed description of the resulting equations of motion. The FVM is covered from its early version of 1963 to the current extended model (2005). Its salient feature is a primary TEV and a counterrotating BV, as part of the 'unsteady Magnus effect'. An intense, beneficial interaction/stabilization (TEV–LEV) is identified, which explains many phenomena in nature and engineering. In case of fixed, inclined AFs, the TEV-driven intermittent suction is shown to maintain an 'average smooth flow condition' at the trailing edge. In general the finite vortex size ($2a/R$) plays a key role, and for oscillating AFs four scaling parameters define the flow (the v_m is used instead of the usual v_∞): $\mathrm{Re}_\mathrm{vmax}$, $\mathrm{Str}_\mathrm{m}, f$ and A_A.

Practical FVM analyses in engineering design and nature include

- an airplane rolling, taking-off and in cruise flight;
- pitching or plunging AF experiments in arbitrary free flow, indicating drag or thrust regimes;
- a complete swimming performance of a large blue whale;
- the take-off and cruise flight of a large heron.

FVM application and validation also cover the comparison with numerous experimental results and NS findings. We summarize the following conclusions:

- The model provides consistent physical explanation of force generation from TEV roll-up. New mechanisms are identified and mathematically formulated; they allow to simulate flows around fixed as well as oscillating AFs.
- A wide range of problems can be solved quickly and efficiently: oscillating AFs with $\mathrm{Re}_\mathrm{R} = 10^3$–$10^6$ and $\mathrm{Str}_\mathrm{A} = 0.03$–$1.70$. Promising results were recently obtained for fixed AFs with $\mathrm{Re}_\mathrm{R} = 10^5$–$10^7$ and Str (based on the AF thickness) = 2.2–5.3. Design by analysis is inspired towards new engineering solutions (AF and trailing edge design); understanding of nature is improved.
- The current code 'fvm-1' approximates forces, loads, circulation and powers for arbitrary AF kinematics and free-stream flows. Force accuracy is within ±20%, when employing a derived semiempirical relation for ($2a/R$).
- The FVM fills a gap in representing a good complement to minimize or avoid large-scale unsteady NS simulations or extensive experiments. It helps to screen and provide efficient designs of experiments.
- Approximations eqn (A) based on the conservation of momentum are limited to inertial type fluid forces only. Nevertheless, they were successfully used to simulate the swimming of fish. They failed, however, to simulate birds' take-off, since circulatory forces $F_{2,1}$ are neglected.
- FVM limitations are due to
  - — the a priori unknown vortex size;
  - — a wake feedback via the induced jet velocity only;

— consideration of one dominating vortex pair only (TEV/BV);
— circulatory forces are referred to the quarter chord point.

Finally future experimental and numerical work are suggested to investigate

- relations of the type $2a/R$ ($\mathrm{Re}_{\mathrm{vmax}}$, $\mathrm{Str}_{\mathrm{m}}$, f, A_{A} and Ma);
- the TEV–LEV interaction; the control of force generation;
- effects of trailing edge geometry and divergence;
- the dynamic profile quality ζ_{dyn}, provide more test data;
- design improvements for AFs, trailing edges and micro air vehicles;
- finish the generalized 2D kinematics for the FVM (‘fvm-2’);
- parallel NS simulations of FVM analyses.

Acknowledgements

This work is a summary of private studies since 1999 with several spin-offs into engineering applications.

The author would like to thank his father, Prof. Wolfgang Liebe, for his inspiring discussions of the physics involved. Many valuable, sometimes controversial, disputes have been a stimulating and continuously creative source of progress.

Prof. Carlos Brebbia, the initiator of the successful series ‘Design and Nature’, always provided help and support from the Wessex Institute of Technology, UK.

In addition, the author gratefully acknowledges comments and verifications from Prof. Wolfgang Zander, Technical University of Berlin. Also the helpful consultations and suggestions from Dr. Günther Walz, Siemens Power Generation, Mülheim, are acknowledged.

Last but not the least, many thanks are given to several contributors of this volume. During our review of their papers we had intense, partly transdisciplinary discussions with a mutual stimulation of ideas: Prof. Peter Freymuth, USA; Prof. Frank Fish, USA; Prof. Anders Hedenström, Sweden; Prof. Keiji Kawachi, Japan; Prof. Max Platzer, USA; and Dr. Volker Simon as well as Prof. Bernhard Weigand from the Technical University of Stuttgart, Germany.

Nomenclature

a	m	radius of finite vortex
A	m^2	cross-sectional or surface area
A_{A}	–	dimensionless amplitude of AF oscillation
b	m	wing span
B	m	extension (length) of the trailing edge along the airfoil
C_{L} ($C_{\mathrm{L,dyn}}$)	–	static (dynamic) lift coefficient, $C_{\mathrm{L}} = F_{\mathrm{L}}/(\rho/2v^2 RB)$
C_{T}	–	thrust coefficient, $C_{\mathrm{T}} = F_{\mathrm{T}}/(\rho/2\, v^2\, RB)$
$C_{\mathrm{D}}(C_{\mathrm{D,dyn}})$	–	static (dynamic) drag coefficient, $C_{\mathrm{D}} = F_{\mathrm{D}}/(\rho/2\, v^2\, RB)$
D	m	maximum effective body cross-section diameter
f, f_∞	–	velocity ratio $= (v_{\mathrm{m}}/v_{\mathrm{max}})$, free stream $f_\infty = (v_\infty/v_{\mathrm{max}})$
$f_{\mathrm{VD}} = f_{\mathrm{OS}}$	Hz	frequency of vortex detachment equal to that of AF oscillation
f_{VS}	Hz	frequency of vortex shedding for fixed body
f_{D}	–	ratio of moments of inertia $= (\theta_{\mathrm{e}}/\theta_{\mathrm{s}})$
$F_{\mathrm{x,y}}$	N	overall forces acting at finite vortex
F_2	N	transverse (Magnus-type or ‘lift’) force on a finite, cylindrical vortex, spinning in the parallel flow v_{R} (F_2 is perpendicular to v_{R})

F_1	N	AF-drag-type force, in-line with v_R and perpendicular to F_2
F_L	N	general lift force
F_T	N	general thrust force
F_D	N	general drag force
F_W	N	overall weight
$H(H_i, H_z)$	N	total (inertial, circulatory) horizontal force component at the AF leading edge
H_{mT}	N	mean total horizontal force at AF over one full cycle T
L, l	m	length
m	kg/s	fluid mass flow
m_B	kg	overall body mass
m_{in} (m_{out})	kg/s	fluid mass flow into (out of) the finite vortex
m_s	kg	mass of AF structure
m_v	kg	mass of finite vortex (cylinder)
$M(M_i, M_z, M_B)$	Nm	total (inertial, circulatory, rotational) bending moment at AF
Ma	–	Mach number $= (v/v_{sound})$
$P(P_i, P_z, P_B)$	W	total (inertial, circulatory, rotational) power required to produce the prescribed AF motion
R, R_{eff}	m	chord of airfoil (plate), effective radius (lever)
r	m	radial coordinate
r_s	m	radius of 'solid' vortex core
$\mathrm{Re} = \mathrm{Re}_R$	–	Reynolds number $= (vR/\nu) = (v_\infty R/\nu)$
Re_{vm}	–	Reynolds number for mean flow thru the oscillating AF $\mathrm{Re}_{vm} = (v_m R/\nu)$
Re_{vmax}	–	Reynolds number for maximum oscillating velocity at AF trailing edge $\mathrm{Re}_{vmax} = (v_{max}\, R/\nu)$; for pure pitching: $\mathrm{Re}_{vmax} = (\varphi_o\, \omega\, R^2/\nu)$
Ri	–	curvature Richardson number
R_c	m	radius of streamline curvature
r, φ, z	–	cylindrical coordinates
s, s_o	m	plunging oscillation s of AF, amplitude of s
Str	–	Strouhal number, natural vortex shedding from the trailing edge thickness Δ of a fixed AF, $\mathrm{Str} = (f_{VS}\Delta/v_\infty)$
Str_D	–	Strouhal number, natural vortex shedding from a fixed circular cylinder, $\mathrm{Str}_D = (f_{VS}\, D/v_\infty)$
Str_R	–	Strouhal number, natural vortex shedding from a fixed AF, $\mathrm{Str}_R = (f_{VS} R/v_\infty)$
Str_∞	–	Strouhal number for an oscillating AF: frequency f_{OS}, $\mathrm{Str}_\infty = (f_{OS}\, R/v_\infty)$
Str_A	–	Strouhal number for a plunging AF: frequency f_{OS} and amplitude s_o, $\mathrm{Str}_A = (f_{OS}\, s_o/v_\infty)$
Str_m	–	modified Strouhal number for an oscillating AF: frequency f_{OS}, $\mathrm{Str}_m = (f_{OS}\, R/v_m)$
$\mathrm{Str}_{A,m}$	–	modified Strouhal number for a plunging AF: frequency f_{OS} and amplitude s_o, $\mathrm{Str}_{A,m} = (f_{OS}\, s_o/v_m)$
t, T	s	time, cycle time $T = 1/f_{OS} = 2\pi/\omega$
$\Delta t_a, \Delta t_f$	s	attachment or residence time of TEV, feeding time of TEV
v, v_∞	m/s	fluid velocity, free-stream velocity
v_m	m/s	Mean flow-through velocity at the quarter chord point M of AF

v_s	m/s	'swimming velocity' of a fish or a 'freely swimming AF'
v_N, v_{max}	m/s	transverse (normal) velocity across the AF trailing edge, maximum velocity of the trailing edge, relative to the fluid
v_F, v_{id}	m/s	flight velocity, induced velocity from vortex detachment at the trailing edge
v_R	m/s	overall resulting incidence flow velocity at the quarter chord point M
v_{PRN}	m/s	transverse (normal) velocity component across the trailing edge of the AF
v_{PR}	m/s	overall resulting incidence flow velocity at point P
$V(V_i, V_z)$	N	total (inertial, circulatory) vertical force component at the AF leading edge
x, y, z	m	Cartesian coordinates
$x_s y_s$	m	instantaneous coordinates of the center of the finite TEV
α (α_{mean})	rad	instantaneous angle of attack (mean angle of attack)
α_{SS} (α_{DS})	rad	static (dynamic) stall angle
α_M (t)	rad	instantaneous angle between $F_1(t)$ and AF chord
β, β_o	rad	plunging or flapping angle of wing, amplitude of β
$\gamma_M(t)$	rad	instantaneous angle between F_2 and the x-axis
γ_{CL}	rad	take-off (climbing) angle of a bird
δ	m	boundary layer thickness
ζ (ζ_{dyn})	–	static (dynamic) profile quality
φ, φ_o	rad	pitching φ of the AF chord, amplitude of φ
φ_m	rad	mean angle of attack
Ø	rad	rotational angle of spinning finite TEV
Γ $(-\Gamma)$	m^2/s	circulation of the attached TEV (the BV around the AF)
θ_s, θ_e	$kg\,m^2$	polar moments of inertia: solid, fluid equivalent [3]
ν	m^2/s	kinematic viscosity of fluid
ψ	rad	phase angle
ρ	kg/m^3	fluid density
ω	s^{-1}	circular frequency of oscillation (rotation)

References

[1] van Dyke, M., *An Album of Fluid Motion*, Parabolic Press: Stanford, USA, 1982.

[2] Liebe, W., *Der Schwanzschlag der Fische*, VDI-Zeitschrift, Bd. 105, Nr.28, VDI-Verlag: Düsseldorf, S.1298–1302, 1963.

[3] Liebe, W. & Liebe, R., Manifestation of the finite vortex—lift, thrust and drag. *Flow Phenomena in Nature*, Vol. 1, WIT: UK, pp. 247–282, 2006.

[4] Liebe,W. & Liebe, R., A general finite vortex model to simulate unsteady aerodynamics in nature. *Int. Conf. Proceedings 'Design & Nature 2002'*, Udine, Italy, September 2002.

[5] Liebe, R., Validation of the finite vortex model by analyzing unsteady aerodynamic experiments. *Int. Conf. Proceedings 'Design & Nature 2002'*, Udine, Italy, September 2002.

[6] Liebe, R., Design and Nature, WIT Seminar, Ashurst Lodge, England, July 2005.

[7] Liebe, R., Applications of the finite vortex model. *Int. Conf. Proceedings, 'Design & Nature 2004'*, Rhodes, Greece, June 2004.

[8] Wood, C.J. & Kirmani, S.F.A., Visualization of heaving airfoil wakes including the effect of a jet flap. *Journal of Fluid Mechanics*, **41**, pp. 627–640, 1970.

[9] Freymuth, P., Gustafson, K.E. & Leben, R., Visualization and computation of hovering mode vortex dynamics. *Vortex Methods and Vortex Motion*, eds. K.E. Gustafson & J.A. Sethian, SIAM: Philadelphia, PA, pp. 143–169, 1991.

[10] Hedenström, A., Vortex wakes of bird flight: old theory, new data and future prospects. *Flow Phenomena in Nature*, Vol. 2, WIT: UK, pp. 706–734, 2006.

[11] Lugt, H., *Wirbelströmung in Natur und Technik*, G. Braun Verlag, 1979.

[12] Koopmann, G.H., The vortex wakes of vibrating cylinders at low Reynolds numbers. *Journal of Fluid Mechanics*, **28**(**3**), pp. 501–512, 1967.

[13] Bublitz, P., The periodic normal force on a circular cylinder in cross-flow—an unsteady Magnus effect. *Z. Flugwiss. Weltraumforschg*., **7**(**4**), pp. 253–262, 1983.

[14] Azuma, A., 2D steady/unsteady wings at low Re number flow. *Flow Phenomena in Nature*, Vol. 1, WIT: UK, pp. 169–192, 2006.

[15] Kuethe, A. *et al*., *Foundations of Aerodynamics*, 4th edn, John Wiley & Sons, 1986.

[16] Platzer, M.P., Jones, K.D., Steady and unsteady aerodynamics. *Flow Phenomena in Nature*, Vol. 2, WIT: UK, pp. 531–541, 2006.

[17] Cebeci, T., Platzer, M.P. *et al*., *Analysis of Low-Speed Unsteady Airfoil Flows*, Horizons Publishing: Springer, 2005.

[18] Rayner, J.M.V., A vortex theory of animal flight. Part 1: The vortex wake of a hovering animal. *Journal of Fluid Mechanics*, **91(4)**, pp. 697–730, 1979.

[19] Lan, C.E., The unsteady quasi-vortex-lattice method with application to animal propulsion. *Journal of Fluid Mechanics*, **93(4)**, pp. 747–765, 1979.

[20] Kamemoto, K., Zhu, B. & Ojima, A., Attractive features of an advanced vortex method and its subjects as a tool of Lagrangian LES. *14th Sympos. on Computat. Fluid Dynamics*, Tokyo, December 2000.

[21] Zbikowski, R., On aerodynamic modeling of an insect-like flapping wing in hover for micro air vehicles. *Philosophical Transactions of the Royal Society of London (Series A)*, **360(1791)**, pp. 273–290, 2002.

[22] Liebe, W., Der Auftrieb am Tragflügel: Entstehung und Zusammenbruch, Aerokurier, Heft 12, S.1520–1523, 1979.

[23] Liebe, R. & Liebe, W., The finite vortex model for unsteady aerodynamics. *International Industrial Conference BIONICS 2004*, Hannover, April 2004, Fortschrittsberichte VDI, Reihe 15, Nr. 249, S.191–199.

[24] Liebe, W. & Liebe, R., Modell, Berechnung und Anwendung periodisch erzeugter Kantenwirbel im Turbomaschinenbau, Patent No. DE 102 37 341 A1 (14.8.2002).

[25] Bechert, D.W., Hage, W. & Meyer, R., Self-adapting flaps on bird and aircraft wings. *Flow Phenomena in Nature*, Vol. 2, WIT: UK, pp. 435–446, 2006.

[26] Bechert, D.W., Meyer, R. & Hage, W., Drag reduction of airfoils with miniflaps. Can we learn from dragonflies? AIAA-2000-2315, Fluids 2000, Denver, June 2000.

[27] Meyer, R.J.K., Experimentelle Untersuchungen von Rückstromklappen auf Tragflügeln zur Beeinflussung von Strömungsablösungen, Dissertation TU-Berlin, 2000.

[28] Rechenberg, I., Bannasch, R. *et al*., Aeroflexible Oberflächenklappen als 'Rückstrombremsen' nach dem Vorbild der Deckfedern des Vogelflügels, Forschungsvorhaben 13N 6536 des BMBF, Statusbericht, 1995.

[29] Platzer, M.P., Jones, K.D. *et al*., Flapping-wing propulsion for a micro-air vehicle, Naval Postgraduate School, AIAA-2001-0126, 39th Aerospace Sciences Meeting, Reno, NV, USA, January 2001.

[30] Schatz, M., Thiele, F., Numerical study of high-lift flow with separation control by periodic excitation, AIAA-2001-0296, 39th AIAA Aerospace Sciences meeting, Reno, NV, USA, January 2001.

[31] Mehta, U.B., Dynamic stall of an oscillating airfoil, Stanford University, Stanford, CA, USA, 1977.

[32] Vermeulen, P.J., Miller, D.N. *et al.*, Ejector pumping enhancement through pulsing primary flow. Proc. of ASME TURBO EXPO 2002, paper GT-2002-30007, Amsterdam, NL, June 2002.

[33] Weaver, D., McAlister, K.W. & Tso, J., Control of VR-7 dynamic stall by strong steady blowing. *Journal of Aircraft*, **41(6)**, pp. 1404–1413, 2004.

[34] Carr, L.W., Progress in analysis and prediction of dynamic stall. *Journal of Aircraft*, **25**, pp. 6–17, 1988.

[35] Lai, J.C.S. & Platzer, M., Characteristics of a plunging airfoil at zero free velocity. *AIAA Journal*, **39(3)**, pp. 531–534, 2000.

[36] Liebe, R., Trailing edge designs for high performance profiles in engineering, Siemens patent, 2006.

[37] Kasper, W.A., Some ideas of vortex lift, Society of Automotive Engineers, Inc., paper no. 750547, 12 pages, ca. 1978.

[38] Freymuth, P., Propulsive vortical signatures of plunging and pitching airfoils. *AIAA Journal*, **26(7)**, pp. 881–883, 1988.

[39] Durst, F., Numerische Strömungs-Simulationen. Info-Schrift vom LSTM, Universität Erlangen-Nürnberg, Germany, 2004.

[40] Dickinson, M.H. & Lehmann, O., Wing rotation and the aerodynamic basis of insect flight. *Science*, **284**, pp. 1954–1960, 1999.

[41] Dickinson, M.H., Unsteady mechanisms of force generation in aquatic and aerial locomotion. *American Zoologist*, **36**, pp. 537–554, 1996.

[42] Kawachi, K., Unsteady wing characteristics at low Reynolds number. *Flow Phenomena in Nature*, Vol. 2, pp. 420–434, 2006.

[43] Panda, J. & Zaman, K.B.M.Q., Experimental investigation of the flow field of an oscillating airfoil and estimation of lift from wake surveys. *Journal of Fluid Mechanics*, **265**, pp. 65–95, 1994.

[44] Spedding, G.R., Rosen, M. & Hedenström, A., A family of vortex wakes generated … free flight … natural range of flight speeds. *Journal of Experimental Biology*, **206**, pp. 2313–2344, 2003.

[45] Liebe, R., Swimming performance of an oscillating hydrofoil propulsor. *International Journal Design & Nature*, to appear.

[46] Didier, F., Denos, R. & Arts, T., Unsteady rotor heat transfer in a transonic turbine stage. *Proc. of ASME TURBO EXPO 2002*, paper GT-2002-30195.

[47] Zheng, X., Zhou, X. & Zhou, S., Investigation on a type of flow control to weaken unsteady separated flows by unsteady excitation in axial flow compressors. *Journal of Turbomachinery*, Trans. ASME, **127**, pp. 489–496, 2005.

[48] Carr, L.W., Mc Alister, K.W. & Mc Croskey, W.J., Analysis of the development of dynamic stall based on oscillating airfoil experiments, NASA TN-D8382, January 1977.

[49] Eck, B., Technische Strömungslehre, 7. Auflage, Springer-Verlag: Berlin, 1966.

[50] Wu, J.H. & Sun, M., Unsteady aerodynamic forces of a flapping wing. Journal of Experimental Biology, **207**, pp. 1137–1150, 2004.

[51] Liu, H., Ellington, C.P., *et al.*, A computational fluid dynamic study of hawkmoth hovering. *Journal of Experimental Biology*, **201**, pp. 461–477, 1998.

[52] Birch, J.M., Dickson, W.B. & Dickinson, M.H., Force production and flow structure of the leading edge vortex on flapping wings at high and low Reynolds numbers. *Journal of Experimental Biology*, **207**, pp. 1063–1072, 2004.

[53] Birch, J.M. & Dickinson, M.H., The influence of wing-wake interactions on the production of aerodynamic forces in flapping flight. *Journal of Experimental Biology*, **206**, pp. 2257–2272, 2003.

[54] Kays, W., Crawford, M. & Weigand, B., *Convective Heat and Mass Transfer*, 4th edn, McGraw Hill: New York, 2005.

[55] Pierce, D., Photographic evidence of formation and growth of vorticity behind plates accelerated from rest in still air. *Journal of Fluid Mechanics*, **11**, pp. 460–464 plus figures, 1961.

[56] Prandtl, L., Über Flüssigkeitsbewegung bei sehr kleiner Reibung, Verhandlungen des III Internat. Math. Kongresses, Heidelberg (August 1904) Teubner Verlag, S.484–491, 1905.

[57] Ahlborn, F., Die Ablösungstheorie der Grenzschichten und die Wirbelbildung. Jahrbuch der Wissenschaftlichen Gesellschaft für Luftfahrt e.V. (WGL), S.171–188, 1927.

[58] Jian, T. & Ke-Qin, Z., Numerical and experimental study of flow structure of low-aspect-ratio wing. *Journal of Aircraft*, **41(5)**, pp. 1196–1201, 2004.

[59] Wang, Z.J., Liu, G.J. & Childress, S., Connection between corner vortices and shear layer instability in flow past an ellipse. *Physics of Fluids*, **11(9)**, pp. 2446–2448, 1999.

[60] Schlichting, H., Grenzschicht-Theorie, 5. Auflage, G. Braun Verlag: Berlin, 1965.

[61] Bublitz, P., Geschichte der Entwicklung der Aeroelastik in Deutschland von den Anfängen bis 1945. DFVLR-Mitteilung 86–25, Köln, 1986.

[62] Ramamurti, R. & Sandberg, W., Simulation of flow about flapping airfoils … finite element flow solver. *AIAA Journal*, **39(2)**, pp. 253–260, 2001.

[63] Gustafson, K., Navier–Stokes computation of hovering dynamics. *Flow Phenomena in Nature*, Vol. 2, WIT: UK, pp. 552–572, 2006.

[64] Weigand, B. & Simon, V., Laws of similarity in fluid mechanics. *Flow Phenomena in Nature*, Vol. 1, WIT: UK, pp. 20–35, 2006.

[65] Lindhe Norberg, U., Flight and scaling of flyers in nature. *Flow Phenomena in Nature*, Vol. 1, WIT: UK, pp. 120–154, 2006.

[66] Pedersen, C.B. & Żbikowski, R., An indicial-Polhamus aerodynamic model of insect-like flapping wings in hover. *Flow Phenomena in Nature*, Vol. 2, WIT: UK, pp. 606–666, 2006.

[67] Liebe, W., Generation and breakdown of aerodynamic lift, Presentation at Hampton, VA, NASA publication, March 1979.

[68] Kompenhans, J., Modern image-based experimental methods for application in fluid dynamics. *Flow Phenomena in Nature*, Vol. 2, WIT: UK, pp. 669–697, 2006.

[69] Ohashi, H. & Ishikawa, N., Visualization study of a flow near the trailing … of airfoil, *Bull. of the Jap. Soc. of Mech. Engrs.*, **15**, pp. 840–845, 1972.

[70] Koochesfahani, M.M., Vortical patterns in the wake of an oscillating airfoil, *AIAA Journal*, **27(9)**, pp. 1200–1205, 1989.

[71] Liebe, W., Die schwingende Hinterkante als Auftriebshilfe und zur Verminderung des Widerstands am Tragflügel, DGLR-Jahrestagung, Berlin, 1999.

[72] Siemens Forum/Bionik-Ausstellung, Broschüre München, May 1999.

[73] Szabo, I., Höhere Technische Mechanik, 2. Auflage, Springer-Verlag: Berlin, 1958.

[74] Jarius, M., Untersuchung einer Axialgitterschaufel mit Höchstumlenkung durch Struktur- und niederfrequente Wölbungsvariation, Dissertation TU-Berlin, 2000.

[75] Sondak, D., Simulation of vortex shedding in a turbine stage, ASME Conf. 1998, paper 98-GT-242.

[76] Schobeiri, T., Recent advances in unsteady boundary layer transition research. *Flow Phenomena in Nature*, Vol. 2, WIT: UK, pp. 573–605, 2006.

[77] Krämer, E., TE-thickness of aircrafts, Personal communication, TU-Stuttgart, July 2005.

[78] Kesel, A., Lernen von den Besten: Innovationspotential aus dem Reich der Insekten, 47. Internat. Wissenschaftl. Kolloquium/TU-Ilmenau, September 2002.

[79] Wagner, H., Über die Entstehung des dynamischen Auftriebs von Tragflügeln. *Zeitschrift für Angewandte Mathematik und Mechanik (ZAMM)*, **5**, S.17–35, 1925.

[80] Liebeck, R.H., Design of subsonic airfoils for high lift. *Journal of Aircraft*, **15(9)**, pp. 547–561, 1978.

[81] Fish, F.E., Diversity, mechanics and performance of natural aquatic propulsors. *Flow Phenomena in Nature*, Vol. 1, pp. 57–87.

[82] Stamhuis, E.J., Shedding light on animal-generated flows: quantitative analysis of animal-generated flow patterns using DPIV. *Flow Phenomena in Nature*, Vol. 2, pp. 735–746, 2006.

[83] Fish, F., Comparative kinematics and hydrodynamics of *Odontoceta cetaceans:* Morphological and ecological correlates with swimming performance. *Journal of Experimental Biology*, **201**, pp. 2867–2877, 1998.

[84] Nachtigall, W., Data on fruit-flies, Personal communication, University of Saarbrücken, May 2005.

[85] Herzog, K., Anatomie und Flugbiologie der Vögel, Gustav Fischer Verlag: Stuttgart, 1968.

[86] Thomas, A.L.R., Insect flight aerodynamics: structure of the leading edge vortex and selection pressures responsible for the use of high lift aerodynamic mechanisms in insects. *Flow Phenomena in Nature*, Vol. 1, pp. 198–206, 2006.

[87] Freymuth, P., Vortex visualizations for two-dimensional models of caudal fin fish propulsion. *Flow Phenomena in Nature*, Vol. 2, pp. 340–356, 2006.

[88] Würz, M. & Repetto, N., *Wale und Delphine, Biografie der Meeressäuger*, Jahr Verlag: Hamburg, 1998.

[89] Johansson, C. & Wetterholm, B., Sea-parrots. *Journal Experimental Biology*, **205**, pp. 371–378, 2002.

[90] Rüppell, G., Vogelflug, Kindler Verlag, 1975.